Electronic Supplementary Material (ESI) for Inorganic Chemistry Frontiers.

Supporting Information

Series of Dysprosium-Based Hydrogen-Bonded Organic Frameworks: Thermally Triggered Off→On Conversion of Single-Ion Magnet

Hai-Ling Wang,[a,+] Xiong-Feng Ma,[a,+] Zhong-Hong Zhu,[a,*] Yi-Quan Zhang,[b,*] Hua-Hong Zou,[a,*] Fu-Pei Liang[a,c,*]

[a]State Key Laboratory for Chemistry and Molecular Engineering of Medicinal Resources, School of Chemistry & Pharmacy of Guangxi Normal University, Guilin 541004, P. R. China. E-mail: fliangoffice@yahoo.com, gxnuchem@foxmail.com

[b]Jiangsu Key Laboratory for NSLSCS, School of Physical Science and Technology, Nanjing Normal University, Nanjing 210023, P. R. China. E-mail: zhangyiquan@njnu.edu.cn

[c]Guangxi Key Laboratory of Electrochemical and Magnetochemical Functional Materials, College of Chemistry and Bioengineering, Guilin University of Technology, Guilin 541004, P. R. China

Supporting Tables	
Table S1	Literature survey for MOFs, COFs, HOFs, MHOFs and Ln-HOFs.
Table S2a	Crystallographic data of the complexes **Cl-1**, **Br-1**, **Br2-1** and **Br3-1**.
Table S2b	Selected bond lengths (Å) and angles (°) of complexes **Cl-1**, **Br-1**, **Br2-1** and **Br3-1**.
Table S3	*SHAPE* analysis of the Dy^{III} ion in **Cl-1**.
Table S4	Hydrogen-bonds and C-Cl···π bonds geometries and π···π interactions for **Cl-1**.
Table S5	*SHAPE* analysis of the Dy^{III} ion in **Br-1**.
Table S6	Hydrogen-bonds and C-Br···π bonds geometries and π···π interactions for **Br-1**.
Table S7	Major species assigned in the HRESI-MS of **Cl-1**, **Cl-2**, **Br-1** and **Br-2** in positive mode and anion mode.
Table S8	Selected parameters from the fitting results of the Cole-Cole plots for **Cl-2** under 0 Oe dc-field.
Table S9~10	Selected parameters from the fitting results of the Cole-Cole plots for **Br-2** and **Br-3** under 0 and 2000 Oe field.
Table S11a	Calculated energy levels (cm^{-1}), $\boldsymbol{g}$ (g_x, g_y, g_z) tensors and predominant m_J values of the lowest eight Kramers doublets (KDs) of four models using CASSCF/RASSI-SO with MOLCAS 8.2.
Table S11b	In wave functions with definite projection of the total moment | *JM* > for the lowest two KDs for four models using CASSCF/RASSI-SO with MOLCAS 8.2.
Table S12a	*SHAPE* analysis of the Dy^{III} ion in **Br2-1**.
Table S12b	Hydrogen-bond and C-Br···π bonds geometries and π···π interactions for **Br2-1**.
Table S13	Major species assigned in the HRESI-MS of **Br2-1** and **Br2-2** in positive mode.
Table S14a	Selected parameters from the fitting results of the Cole-Cole plots for **Br2-2** under 2000 Oe field.
Table S14b	Selected parameters from the fitting results of the Cole-Cole plots for **Br2-3** under 2000 Oe field.
Table S15a	Calculated energy levels (cm^{-1}), $\boldsymbol{g}$ (g_x, g_y, g_z) tensors and predominant m_J values of the lowest eight Kramers doublets (KDs) of five models using CASSCF/RASSI-SO with MOLCAS 8.2.
Table S15b	In wave functions with definite projection of the total moment | *JM* > for the lowest two KDs for five models using CASSCF/RASSI-SO with MOLCAS 8.2.
Table S16	*SHAPE* analysis of the Dy^{III} ion in **Br3-1**.
Table S17	Hydrogen-bond and C-Br···π bonds geometries and π···π interactions for **Br3-1**.
Table S18	Selected parameters from the fitting results of the Cole-Cole plots for **Br3-1** under 2000 Oe field.
Table S19	Selected parameters from the fitting results of the Cole-Cole plots for **Br3-3** under 2000 Oe field.
Supporting Figures	
Figure S1a	Intermolecular interactions in the structure of **Cl-1**.
Figure S1b	The space filling of organic molecules in axial a for Dy-HOFs (**Cl-1** and **Br-1**).
Figure S1c	Hirshfeld surfaces mapped with d_{norm} (a, d and e) showing Shape-index (b) and Curvedness (c) for the **Cl-1**.
Figure S2	Intermolecular interactions in the structure of **Br-1**.
Figure S3	Hirshfeld surfaces mapped with d_{norm} (a) showing Shape-index (b) and Curvedness (c) for the **Br-1**.
Figure S4	The connecting modes of the clusters through C–Cl/Br···π, π···π interactions and/or hydrogen bonds for **Cl-1** and **Br-1**.
Figure S5a	The PXRD data for **Cl-1** and **Cl-2**.
Figure S5b	The PXRD data for **Br-1** and **Br-2**.

Figure S5c~5f	The superposed simulated and observed spectra of several species for **Cl-1**, **Cl-2**, **Br-1** and **Br-2** (positive mode).
Figure 5g	HRESI-MS of a series of Dy-HOFs in negative mode: **Cl-1** (top in a), **Cl-2** (bottom in a), **Br-1** (top in b), and **Br-2** (bottom in b).
Figure 5h~5k	The superposed simulated and observed spectra of several species for **Cl-1**, **Cl-2**, **Br-1** and **Br-2** (negative mode).
Figure S6	Ultraviolet-visible absorption spectrum (a/d) and fluorescence spectrum (b/e and c/f) of **Cl-1/Br-1** and **Cl-2/Br-2**.
Figure S7	Temperature dependence of $\chi_m T$ for a series of Dy-HOFs.
Figure S8a	Field dependence of the magnetization for **Cl-1**, **Cl-2**, **Cl-3** (a-c) and **Br-1**, **Br-2**, **Br-3** (d-f) at 2-6 K.
Figure S8b	Hysteresis loops for a series of Dy-HOFs at 2 K.
Figure S9	Variable-frequency dependent ac susceptibilities under 0 Oe field for **Cl-2**.
Figure S10a	Variable-frequency dependent ac susceptibilities and Cole-Cole plots from ac-susceptibilities for **Br-2** under 0 and 2000 Oe dc-field.
Figure S10b	Arrhenius plots generated from the temperature dependent relaxation times extracted from the ac-susceptibilities Cole-Cole fits for **Br-2** in H_{dc} = 2000 Oe.
Figure S11	The temperature dependence of the in-phase (χ') and out-of-phase (χ'') ac-susceptibilities for different frequencies in 0 and 2000 Oe dc-field for **Cl-3** (a and b) and **Br-3** (c and d).
Figure S12	Variable-frequency dependent ac susceptibilities and Cole-Cole plots from ac-susceptibilities for **Br-3** under 0 and 2000 Oe dc-field.
Figure S13	Arrhenius plots generated from the temperature dependent relaxation times extracted from the ac-susceptibilities Cole-Cole fits for **Br-3** in H_{dc} = 0 Oe and H_{dc} = 2000 Oe.
Figure S14a	Calculated structures of four models—**Cl-1** (a), **Cl-2** (b), **Br-1** (c), **Br-2** (d); H atoms are omitted.
Figure S14b	Calculated orientations of the local main magnetic axes of the ground KDs on Dy^{III} ions of four models—**Cl-1** (a), **Cl-2** (b), **Br-1** (c), **Br-2** (d)
Figure S15a	Intermolecular interactions in the structure of **Br2-1**.
Figure S15b	Hirshfeld surfaces mapped with d_{norm} (a and d) showing Shape-index (b) and Curvedness (c) for the **Br2-1**.
Figure S16a	Thermogravimetry of **Br2-1** at a heating rate of 5 °C/min under N_2 atmosphere.
Figure S16b	HRESI-MS of **Br2-1** (top) and **Br2-2** (bottom).
Figure S16c~S16d	The superposed simulated and observed spectra of several species for **Br2-1** and **Br2-2** (positive mode).
Figure S16e	HRESI-MS of **Br2-1** (top) and **Br2-2** (bottom) in negative mode.
Figure S16f~S16g	The superposed simulated and observed spectra of several species for **Br2-1** and **Br2-2** (negative mode).
Figure S16h	The PXRD data for **Br2-1** and **Br2-2**.
Figure S17	Temperature dependence of $\chi_m T$ for **Br2-1**, **Br2-2**, **Br2-3**.
Figure S18	Field dependence of the magnetization for **Br2-1** (a), **Br2-2** (b) and **Br2-3** (c) at 2-6 K.
Figure S19	The temperature dependence of the in-phase (χ') and out-of-phase (χ'') ac-susceptibilities for different frequencies in 0 and 2000 Oe dc-field for **Br2-1** (a and d), **Br2-2** (c and f) and **Br2-3** (b and e).
Figure S20a	Variable-frequency dependent ac susceptibilities and Cole-Cole plots from ac-susceptibilities for **Br2-2** (a, b and c) under 0 Oe dc-field, and Arrhenius plots generated from the temperature

	dependent relaxation times extracted from the ac-susceptibilities Cole-Cole fits for **Br2-2** (d) and **Br2-3** (d).
Figure S20b	Variable-frequency dependent ac susceptibilities and Cole-Cole plots from ac-susceptibilities for **Br2-3** under 0 dc-field (a and b) and 2000 Oe dc-field (d and e), and Arrhenius plots generated from the temperature dependent relaxation times extracted from the ac-susceptibilities Cole-Cole fits for **Br2-3** (c and f).
Figure S21	(a) Calculated structures of **Br2-2**; H atoms are omitted; (b) Calculated orientations of the local main magnetic axes of the ground KDs on DyIII ions of **Br2-2**; (c) The magnetization blocking barriers in **Br2-2**. The thick black lines represent the KDs as a function of their magnetic moments along the magnetic axis.
Figure S22	Intermolecular interactions in the structure of **Br3-1**.
Figure S23	Thermogravimetry of **Br3-1** at a heating rate of 5 °C/min under N_2 atmosphere.
Figure S24	Temperature dependence of $\chi_m T$ for **Br3-1** and **Br2-3**.
Figure S25	Field dependence of the magnetization for **Br3-1** (a) and **Br3-3** (b) at 2-6 K.
Figure S26	The temperature dependence of the in-phase (χ') and out-of-phase (χ'') ac-susceptibilities for different frequencies in 0 and 2000 Oe dc-field for **Br3-1** (a and c) and **Br3-3** (b and d).
Figure S27	Variable-frequency dependent ac susceptibilities and Cole-Cole plots from ac-susceptibilities for **Br3-1** (a, b and c) under 2000 Oe dc-field, and Arrhenius plots generated from the temperature dependent relaxation times extracted from the ac-susceptibilities Cole-Cole fits for **Br3-1** (d).
Figure S28	Variable-frequency dependent ac susceptibilities and Cole-Cole plots from ac-susceptibilities for **Br3-3** (a, b and c) under 2000 Oe dc-field, and Arrhenius plots generated from the temperature dependent relaxation times extracted from the ac-susceptibilities Cole-Cole fits for **Br3-3** (d).

Experimental Procedures

Materials and Measurements.

All reagents are obtained from commercial sources and can be used without further purification. Elemental analysis (C, H, N) was measured on an Elementar Micro cube elemental analyzer. Thethermal analysis was performed in N_2 at a heating rate of 5 °C/min using Labsys Evo TG-DTG/DSC. IR spectra with KBr pelletwere recorded on PE Spectrum Two FT/IR spectrometer (400−4,000 cm^{-1}). PXRD measurements were recorded on Rigaku D/max-IIIA diffractometer. The magnetic susceptibility was measured by MPMS SQUID-XL magnetometer in the temperature range of 2−300 K. The diamagnetic corrections were estimated using Pascal's constants. Alternating current (AC) susceptibility was measured and the data were collected by increasing temperature from 2 K to 10 K within frequencies ranging from 1 to 1,000 Hz and a drive frequency of 2.5 Oe.

Single-crystal X-ray crystallography.

Diffraction data for all complexes were measured on a Bruker SMART CCD diffractometer (Mo Kα radiation and λ = 0.71073 Å) in Φ and ω scan modes. All structures were solved by direct methods, followed by difference Fourier syntheses, and then refined by full-matrix least-squares techniques on F^2 using SHELXL.[1] All other non-hydrogen atoms were refined with anisotropic thermal parameters. Hydrogen atoms were placed in the calculated position and refined in the isotropic direction using a riding model. Table S2 summarizes X-ray crystallographic data and refinement details for the complexes. Full details can be found in the CIF files provided in the **Supporting Information**. The CCDC reference numbers are 1888145 for **Cl-1**, 1888147 for **Br-1**, 1888146 for **Br2-1** and

1888148 for **Br3-1**.

High resolution electrospray mass spectrometry (HRESI-MS) test.

HRESI-MS were measured at the capillary temperature of 275 °C, and the solution was injected at the rate of 0.3 mL/h. The HRESI-MS used for the measurements was a ThermoExactive, and the data were collected in positive and negative ion modes. The spectrometer was previously calibrated with the standard tune mix to give a precision of *ca*. 2 ppm within the region of 200−2,000 *m/z*. The capillary voltage was 50 V, the tube lens voltage was 150 V, and the skimmer voltage was 25 V. The in-source energy was set within the range of 0−100 eV with a gas flow rate at 10% of the maximum.

Synthesis of Cl-1, **Br-1**, **Br2-1** and **Br3-1.**

Cl-1: 5,7-dichloro-2-methyl-8-quinolinol (0.1 mmol), 2,9-dimethyl-1,10-phenanthroline (0.2 mmol), $Dy(NO_3)_3{\cdot}6H_2O$ (0.1 mmol), MeOH (0.75 mL), CH_3CN (0.75 mL), and 10 μL Et_3N were added in a Pyrex tube. The mixture was heated for 2 days at 80 °C and cooled to room temperature to produce yellow crystals of complex **Cl-1** in 69% yield. Anal. Calcd for $C_{45}H_{34}Cl_6DyN_5O_4$: C, 49.86; H, 3.16; N, 6.46; Found: C, 49.61; H, 3.25; N, 6.60. IR (KBr, cm^{-1}): 3455 (m), 2340 (w), 1545 (s), 1485 (s), 1436 (s), 1370 (w), 1262 (s), 1100 (s), 1021 (m), 869 (m), 730 (s).

Br-1: 5,7-dibromo-2-methyl-8-quinolinol (0.1 mmol), 2,9-dimethyl-1,10-phenanthroline (0.2 mmol), $Dy(NO_3)_3{\cdot}6H_2O$ (0.1 mmol), MeOH (0.75 mL), CH_3CN (0.75 mL), and 15 μL Et_3N were added in a Pyrex tube. The mixture was heated for 2 days at 80 °C and cooled to room temperature to produce yellow crystals of complex **Br-1** in 61% yield. Anal. Calcd for $C_{45}H_{34}Br_6DyN_5O_4$: C, 40.01; H, 2.54; N, 5.18; Found: C, 39.74; H, 2.89; N, 5.23. IR (KBr, cm^{-1}): 3447 (m), 2348 (w), 1547 (s), 1485 (s), 1433 (s), 1361 (w), 1262 (s), 1097 (s), 1023 (m), 867 (m), 735 (s).

Br2-1: 5,7-dibromo-2-methyl-8-quinolinol (0.1 mmol), 2,9-dimethyl-1,10-phenanthroline (0.3 mmol), $Dy(NO_3)_3{\cdot}6H_2O$ (0.1 mmol), MeOH (1.5 mL), and 10 μL Et_3N were added in a Pyrex tube. The mixture was heated for 2 days at 80 °C and cooled to room temperature to produce yellow crystals of complex **Br2-1** in 61% yield. Anal. Calcd for $C_{39}H_{35}Br_2DyN_8O_{11}$: C, 42.05; H, 3.17; N, 10.06; Found: C, 42.28; H, 3.02; N, 10.17. IR (KBr, cm^{-1}): 3448 (m), 2343 (w), 1542 (s), 1486 (s), 1437 (s), 1371 (w), 1263 (s), 1097 (s), 1025 (m), 870 (m), 733 (s).

Br3-1: 5,7-dibromo-2-methyl-8-quinolinol (0.1 mmol), 2-methylquinoline (0.3 mmol, L^3), $DyCl_3{\cdot}6H_2O$ (0.1 mmol), MeOH (0.75 mL), CH_3CN (0.75 mL), and 15 μL Et_3N were added in a Pyrex tube. The mixture was heated for 2 days at 80 °C and cooled to room temperature to produce yellow crystals of complex **Br3-1** in 66% yield. Anal. Calcd for $C_{40}H_{28}Br_6ClDyN_4O_3$: C, 37.24; H, 2.19; N, 4.34; Found: C, 37.01； H, 2.38； N, 4.14. IR (KBr, cm^{-1}): 3446 (m), 2342 (w), 1548 (s), 1484 (s), 1438 (s), 1366 (w), 1261 (s), 1098 (s), 1024 (m), 871 (m), 735 (s).

Synthesis of Cl-2, **Br-2** and **Br2-2.**

The desolvation temperatures of **Cl-2** and **Br-2** were first setted according to the thermogravimetric analysis of the complexes (Figure 2). The yellow crystals of **Cl-1** and **Br-1** (~20 mg for each complex) then were taken in an Al_2O_3 crucible, which was heated from room temperature to 255 and 260 °C, respectively, under flowing nitrogen. Keeping the temperature constant for 2 h, the corresponding desolvated samples **Cl-2** and **Br-2** were obtained. Anal. Calcd for $C_{31}H_{22}Cl_6DyN_3O_4$ (**Cl-2**): C, 42.52; H, 2.53; N, 4.80; Found: C, 42.39; H, 2.81; N, 4.75. IR (KBr, cm^{-1}): 3450 (m), 2342 (w), 1543 (s), 1485 (s), 1437 (s), 1369 (w), 1263 (s), 1099 (s), 1023 (m), 868 (m), 734 (s). Anal. Calcd for $C_{31}H_{22}Br_6DyN_3O_4$ (**Br-2**): C, 32.59; H, 1.94; N, 3.68; Found: C, 32.34; H, 2.13; N, 3.53. IR (KBr, cm^{-1}): 3450 (m), 2342 (w), 1543 (s), 1485 (s), 1437 (s), 1369 (w), 1263 (s), 1099 (s), 1023 (m), 868 (m), 734 (s). The preparation of

complex **Br2-2** was similar to that of complex **Cl-2**. Anal. Calcd for $C_{25}H_{23}Br_2DyN_6O_{11}$: C, 33.15; H, 2.56; N, 9.28; Found: C, 33.42; H, 2.79; N, 10.01. IR (KBr, cm^{-1}): 3450 (m), 2342 (w), 1543 (s), 1485 (s), 1437 (s), 1369 (w), 1263 (s), 1099 (s), 1023 (m), 868 (m), 734 (s).

Synthesis of Cl-3, Br-3, Br2-3 and Br3-3.

Syntheses of **Cl-3, Br-3, Br2-3** and **Br3-3** were performed under aerobic conditions following the same procedure. Take **Cl-3** as an example, about 20 mg **Cl-1** and put it into the mortar, grind and transfer into the mould, and further press samples on the hydraulic press with 25 kPa pressure, the corresponding samples **Cl-3** was obtained.

Table S1. Literature survey for MOFs, COFs, HOFs, MHOFs and Ln-HOFs.

Key words	Number of articles
Metal–organic frameworks (MOFs)[a]	602669
Covalent organic frameworks (COFs)[b]	2778
Hydrogen-Bonded Organic Frameworks (HOFs)[c]	30
Metal-Hydrogen Bonded Organic Frameworks (MHOFs)[d]	3
Ln-Hydrogen Bonded Organic Frameworks (Ln-HOFs)	**1**

[a] Using "Metal–organic frameworks" for topic search in "Scifinder" database from 1950 to Dec. 31, 2018. 602669 papers were found; [b] using "Covalent organic frameworks" for topic search in "Scifinder" database from 1960 to Dec. 31, 2018. 2778 papers were found; [c] using "Hydrogen-Bonded Organic Frameworks" for topic search in "Scifinder" database from 1960 to Dec. 31, 2018. 30 papers were found; and [d] using "Metal-Hydrogen Bonded Organic Frameworks" for topic search in "Scifinder" database from 1960 to Dec. 31, 2018. Only 3 papers were found.

Table S2a. Crystallographic data of the complexes **Cl-1**, **Br-1**, **Br2-1** and **Br3-1**.

Complex	**Cl-1**	**Br-1**	**Br2-1**	**Br3-1**
Formula	$C_{45}H_{34}Cl_6DyN_5O_4$	$C_{45}H_{34}Br_6DyN_5O_4$	$C_{39}H_{35}Br_2DyN_8O_{11}$	$C_{40}H_{28}Br_6ClDyN_4O_3$
Formula weight	1083.97	1350.73	1114.07	1290.07
T (K)	150.0	293.15	150.0	293.15
Crystal system	Monoclinic	Monoclinic	Monoclinic	Monoclinic
Space group	$P2_1/c$	$P2_1/c$	$P2_1/n$	$P2_1/c$
a (Å)	17.4552(5)	18.39(4)	10.3824(5)	17.7059(6)
b (Å)	10.5988(3)	11.17(2)	18.8386(11)	18.3642(4)
c (Å)	24.3721(6)	25.90(5)	21.0988(13)	13.6199(4)
α (°)	90.00	90.00	90.00	90.00
β (°)	109.2150(10)	108.69(3)	99.618(2)	111.014(4)
γ (°)	90.00	90.00	90.00	90.00
V (Å^3)	4257.7(2)	5037(17)	4068.7(4)	4134.0(2)
Z	4	4	4	4
D_c (g cm^{-3})	1.691	1.781	1.819	2.073
μ (mm^{-1})	2.183	6.287	3.872	7.715
Reflns coll.	54559	38101	55058	28403
Unique reflns	8746	8866	7991	7701

R_{int}	0.0910	0.0704	0.0849	0.0431
$^{a}R_1$ [$I \geq 2\sigma(I)$]	0.0378	0.0417	0.0407	0.0334
$^{b}wR_2$ (all data)	0.0913	0.1310	0.1050	0.0712
GOF	1.054	1.017	1.084	1.063

$^{a}R_1 = \Sigma||F_o|-|F_c||/\Sigma|F_o|$, $^{b}wR_2 = [\Sigma w(F_o^2-F_c^2)^2/\Sigma w(F_o^2)^2]^{1/2}$

Table S2b. Selected bond lengths (Å) and angles (°) of complexes **Cl-1**, **Br-1**, **Br2-1** and **Br3-1**.

Cl-1					
Bond lengths (Å)					
Dy1—O2	2.286 (5)	Dy1—O4	2.433 (5)	Dy1—N1	2.733 (6)
Dy1—O1	2.269 (5)	Dy1—N2	2.657 (6)	Dy1—N3	2.761 (6)
Dy1—O3	2.333 (5)				
Bond angles (°)					
O2—Dy1—O3	128.20 (18)	O1—Dy1—O4	96.57 (19)	O3—Dy1—N3	64.86 (18)
O2—Dy1—O4	116.1 (2)	O1—Dy1—N2	89.75 (19)	O4—Dy1—N2	168.48 (15)
O2—Dy1—N2	66.83 (19)	O1—Dy1—N1	65.59 (19)	O4—Dy1—N1	76.05 (18)
O2—Dy1—N1	80.84 (18)	O1—Dy1—N3	153.99 (16)	O4—Dy1—N3	78.3 (2)
O2—Dy1—N3	78.44 (19)	O3—Dy1—O4	91.6 (2)	N2—Dy1—N1	115.40 (19)
O1—Dy1—O2	125.56 (18)	O3—Dy1—N2	78.7 (2)	N2—Dy1—N3	91.9 (2)
O1—Dy1—O3	90.1 (2)	O3—Dy1—N1	150.66 (15)	N1—Dy1—N3	135.26 (18)
Br-1					
Bond lengths (Å)					
Dy1—O2	2.214 (3)	Dy1—O4	2.351 (3)	Dy1—N2	2.568 (3)
Dy1—O1	2.205 (3)	Dy1—N1	2.597 (3)	Dy1—N3	2.626 (4)
Dy1—O3	2.247 (3)				
Bond angles (°)					
O2—Dy1—O3	130.03 (10)	O1—Dy1—O4	99.42 (11)	O3—Dy1—N3	66.42 (11)
O2—Dy1—O4	113.59 (12)	O1—Dy1—N1	67.31 (11)	O4—Dy1—N1	75.75 (11)
O2—Dy1—N1	79.60 (10)	O1—Dy1—N2	88.61 (11)	O4—Dy1—N2	168.05 (11)
O2—Dy1—N2	67.59 (11)	O1—Dy1—N3	154.09 (11)	O4—Dy1—N3	77.35 (11)
O2—Dy1—N3	78.22 (11)	O3—Dy1—O4	92.41 (12)	N1—Dy1—N3	134.26 (11)
O1—Dy1—O2	125.21 (11)	O3—Dy1—N1	150.08 (11)	N2—Dy1—N1	115.75 (11)
O1—Dy1—O3	88.25 (11)	O3—Dy1—N2	78.91 (11)	N2—Dy1—N3	91.55 (11)
Br2-1					
Bond lengths (Å)					
Dy1—O1	2.214 (4)	Dy1—O11	2.457 (4)	Dy1—O3	2.403 (14)
Dy1—O13	2.339 (4)	Dy1—N1	2.538 (4)	Dy1—O10	2.429 (4)
Dy1—O2	2.479 (4)	Dy1—O8	2.486 (8)	Dy1—O6	2.505 (5)
Bond angles (°)					
O1—Dy1—O13	88.37 (14)	O13—Dy1—O10	127.30 (14)	O11—Dy1—O4	148.3 (2)
O1—Dy1—O2	76.18 (14)	O13—Dy1—O6	72.61 (16)	O10—Dy1—O2	70.79 (14)
O1—Dy1—O11	77.71 (15)	O13—Dy1—O8	112.9 (2)	O10—Dy1—O11	52.18 (14)
O1—Dy1—N1	68.43 (14)	O13—Dy1—O4	126.3 (2)	O10—Dy1—N1	138.24 (14)

O1—Dy1—O10	77.59 (14)	O2—Dy1—N1	77.94 (14)	O10—Dy1—O6	120.98 (16)
O1—Dy1—O6	158.97 (15)	O2—Dy1—O6	117.51 (17)	O10—Dy1—O8	68.4 (2)
O1—Dy1—O8	146.0 (2)	O2—Dy1—O8	91.2 (2)	O10—Dy1—O4	103.8 (2)
O1—Dy1—O4	121.1 (2)	O2—Dy1—O4	51.3 (2)	O6—Dy1—N1	97.66 (17)
O13—Dy1—O2	153.45 (15)	O11—Dy1—O2	120.88 (15)	O6—Dy1—O4	67.1 (2)
O13—Dy1—O11	75.31 (15)	O11—Dy1—N1	135.91 (15)	O8—Dy1—N1	140.3 (2)
O13—Dy1—N1	76.31 (14)	O11—Dy1—O6	105.1 (2)	O8—Dy1—O6	53.8 (2)
O4—Dy1—N1	75.5 (2)	O11—Dy1—O8	82.4 (2)	O8—Dy1—O4	68.2 (3)
Br3-1					
Bond lengths (Å)					
Dy1—Cl1	2.6822 (11)	Dy1—O2	2.207 (3)	Dy1—N3	2.625 (3)
Dy1—O3	2.207 (3)	Dy1—N1	2.609 (3)	Dy1—N2	2.583 (3)
Dy1—O1	2.247 (3)				
Bond angles (°)					
O3—Dy1—Cl1	97.34 (8)	O1—Dy1—N3	146.16 (10)	O2—Dy1—N2	66.94 (11)
O3—Dy1—O1	84.42 (10)	O1—Dy1—N2	78.52 (11)	N1—Dy1—Cl1	80.54 (8)
O3—Dy1—N1	150.71 (11)	O2—Dy1—Cl1	118.51 (8)	N1—Dy1—N3	139.47 (10)
O3—Dy1—N3	66.71 (10)	O2—Dy1—O3	124.06 (11)	N3—Dy1—Cl1	78.25 (8)
O3—Dy1—N2	89.57 (10)	O2—Dy1—O1	133.29 (10)	N2—Dy1—Cl1	165.00 (8)
O1—Dy1—Cl1	88.87 (8)	O2—Dy1—N1	80.84 (11)	N2—Dy1—N1	86.91 (11)
O1—Dy1—N1	66.39 (11)	O2—Dy1—N3	79.60 (10)	N2—Dy1—N3	116.75 (11)

In the Dy-HOFs structure, the seven-coordinated Dy(III) cores are surrounded by three nitrogen atoms and three oxygen atoms from three 5,7-dichloro-2-methyl-8-quinolinol (or 5,7-dibromo-2-methyl-8-quinolinol) ligands and one oxygen atom from one coordinated methanol (Figure 1). The bond distances between Dy(III) ion and ligand nitrogen atoms fall in range of 2.569-2.627 Å for **Cl-1** and 2.657-2.763 Å for **Br-1** approximately, the bond distances fall in range of 2.205-2.247 Å for **Cl-1** and 2.269-2.334 Å for **Br-1** between Dy(III) ion and ligand oxygen atoms, and the bond length between Dy(III) ion and oxygen atom from coordinative methanol is 2.350 and 2.439 Å for **Cl-1** and **Br-1** (Table S2).

Table S3. *SHAPE* analysis of the Dy^{III} ion in **Cl-1**.

Label	Shape	Symmetry	Distortion(τ)
HP-7	D_{7h}	Heptagon	31.759
HPY-7	C_{6v}	Hexagonal pyramid	17.062
PBPY-7	D_{5h}	Pentagonal bipyramid	5.794
COC-7	C_{3v}	Capped octahedron	3.439
CTPR-7	C_{2v}	Capped trigonal prism	2.143
JPBPY-7	D_{5h}	Johnson pentagonal bipyramid J13	10.113
JETPY-7	C_{3v}	Johnson elongated triangular pyramid J7	16.384

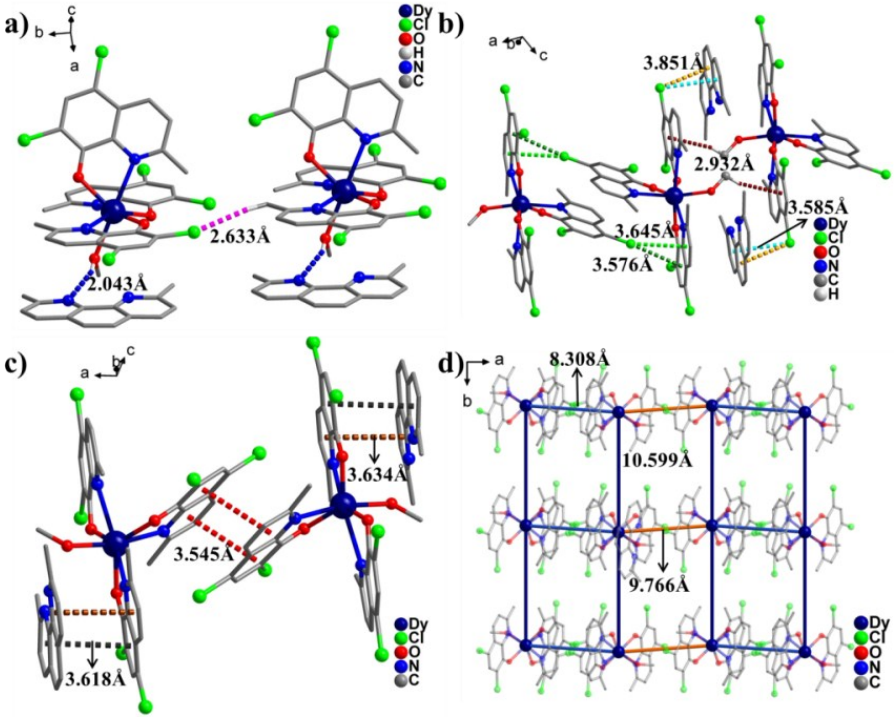

Figure S1a. Intermolecular interactions in the structure of **Cl-1**. (a) O_4-H_4···N_4 (blue dotted line) and C_1-H_{1B}···Cl_2 (pink dotted line); (b) C-Cl···π (turquoise, green, light orange or bright green dotted line) and C-H···π (dark red dotted line); (c) π(Ph or PhC_5N)···π(PhC_5N) (black, brown or red dotted line); (d) connecting cluster to cluster (orange, dark blue or light blue line). Ph: benzene ring, PhC_5N: pyridine ring.

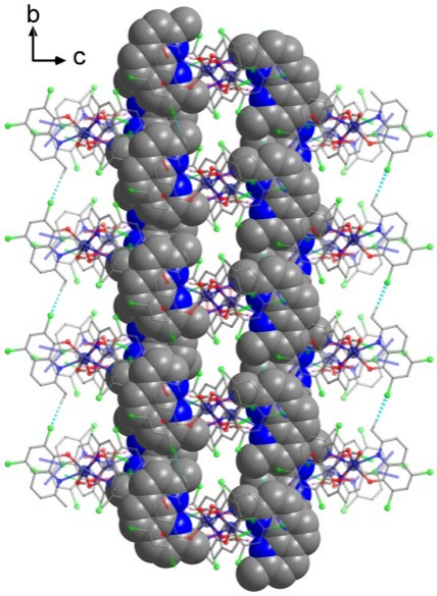

Figure S1b. The space filling of organic molecules in axial a for Dy-HOFs (**Cl-1** and **Br-1**).

Table S4. Hydrogen-bonds and C-Cl···π bonds geometries and π···π interactions for **Cl-1**.

Hydrogen bond	**Distance[a], Å**	**Angle[b], °**
O_4–H_4···N_5	2.043	156
C_1–H_{1B}···Cl_2	2.633	167
π···π	**Distance[c], Å**	**Distance[d], Å**
π(Ph)···π(PhC_5N)	3.545(3)	3.395(3)
π(Ph)···π(PhC_5N)	3.618(3)	3.434(2)
π(PhC_5N)···π(PhC_5N)	3.634(3)	3.465(2)
C–X···π	**Distance[c], Å**	**Angle[e], °**
C_{31}-H_{31A}···π(Ph)	2.932(2)	164
C_{16}–Cl_3···π(PhC_5N)	3.645(2)	160.1
C_{16}–Cl_3···π(Ph)	3.576(2)	157.9
C_{26}–Cl_5···π(PhC_5N)	3.585(3)	88.6
C_{26}–Cl_5···π(Ph)	3.851(3)	105.9

[a] Distance between acceptor and donor; [b] Angle of acceptor–hydrogen–donor; [c] Centroid–to–centroid distance; [d] Interplanar distance; [e] Angle of carbon–hydrogen–centroid.

Hirshfeld surface analysis. CrystalExplorer is a versatile and powerful tool for the analysis of crystal structures. It provides a visual way to explore the interactions of molecular crystals using the Hirshfeld surface and the fingerprint plot. The Hirshfeld surface is mapped with d_{norm} (the normalized contact distance), which is normalized from d_e (the nearest external distance), d_i (the nearest internal distance) and the van der Waals (vdW) radii of the two atoms to the surface:[2, 3]

$$d_{norm} = (d_i - r_i^{vdW})/(r_i^{vdW}) + (d_e - r_e^{vdW})/(r_e^{vdW})$$

While the fingerprint plot is derived from the Hirshfeld surface, these 2D fingerprint plots provide a visual summary of the frequency of each combination of d_e and d_i across the surface of a molecule, [4] so they not only indicate which intermolecular interactions are present, but also the relative area of the surface corresponding to each kind of interaction.

In order to understand the intermolecular interaction of the eutectic formed by the free phenanthroline and the complex, the Hirshfeld surface calculation was performed on the eutectic fragments formed by the free phenanthroline and the complex. From the Hirshfeld surface calculation results, it can be seen that there are mainly three different supramolecular weak interactions between the free phenanthroline and the complex. They are O_4-H_4···N_5, π···π and Cl/Br···π for **Cl-1** (Figure S1c) and **Br-1** (Figure S3).

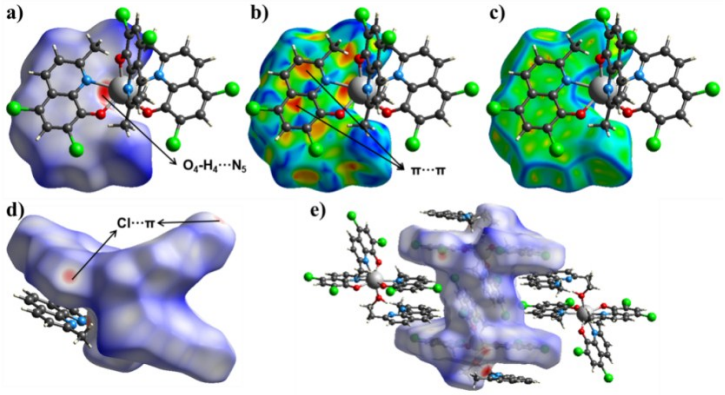

Figure S1c. Hirshfeld surfaces mapped with d_{norm} (a, d and e) showing Shape-index (b) and Curvedness (c) for the **Cl-1**.

Table S5. *SHAPE* analysis of the Dy^{III} ion in **Br-1**.

Label	Shape	Symmetry	Distortion(τ)
HP-7	D_{7h}	Heptagon	32.757
HPY-7	C_{6v}	Hexagonal pyramid	17.045
PBPY-7	D_{5h}	Pentagonal bipyramid	5.528
COC-7	C_{3v}	Capped octahedron	3.262
CTPR-7	C_{2v}	Capped trigonal prism	2.033
JPBPY-7	D_{5h}	Johnson pentagonal bipyramid J13	9.933
JETPY-7	C_{3v}	Johnson elongated triangular pyramid J7	16.254

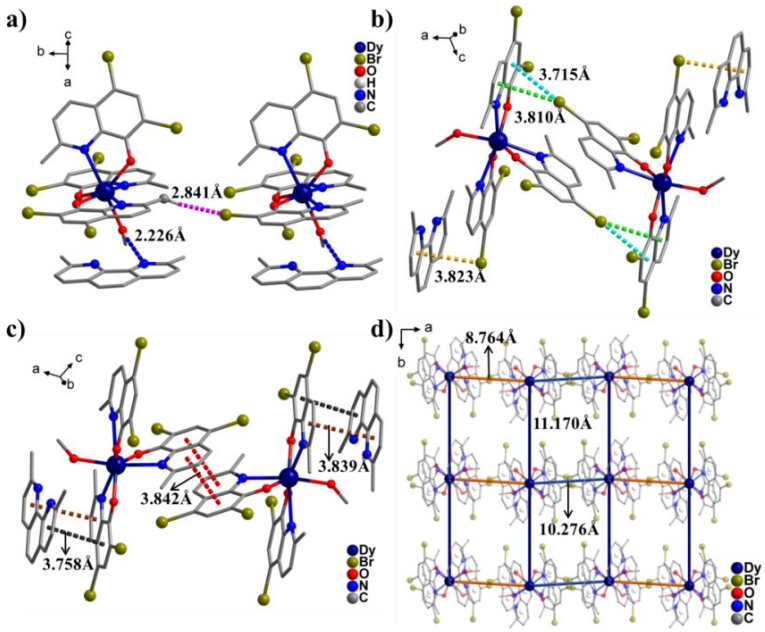

Figure S2. Intermolecular interactions in the structure of **Br-1**. (a) O_4-H_4···N_5 (blue dotted line) and C_1-H_{1B}···Br_2 (pink dotted line); (b) C-Br···π (light orange, bright green or turquoise dotted line); (c) π(Ph or PhC_5N)···π(PhC_5N) (black, brown or red dotted line); (d) connecting cluster to cluster (orange, dark blue or light blue line).

Table S6. Hydrogen-bonds and C-Br···π bonds geometries and π···π interactions for **Br-1**.

Hydrogen bond	**Distance[a], Å**	**Angle[b], °**
O_4–H_4···N_5	2.226	168
C_1–H_{1B}···Br_2	2.841	173
π···π	**Distance[c], Å**	**Distance[d], Å**
π(PhC_5N)···π(PhC_5N)	3.839(9)	3.582(3)
π(Ph)···π(PhC_5N)	3.842(9)	3.657(3)
π(Ph)···π(PhC_5N)	3.758(9)	3.626(3)
C–H···π	**Distance[c], Å**	**Angle[e], °**
C_{16}–Br_3···π(PhC_5N)	3.810(9)	157.9(2)
C_{16}–Br_3···π(Ph)	3.715(9)	157.8(2)
C_{26}–Br_5···π(PhC_5N)	3.823(9)	88.0(2)

[a]Distance between acceptor and donor; [b]Angle of acceptor–hydrogen–donor; [c]Centroid–to–centroid distance; [d] Interplanar distance; [e]Angle of carbon–hydrogen–centroid.

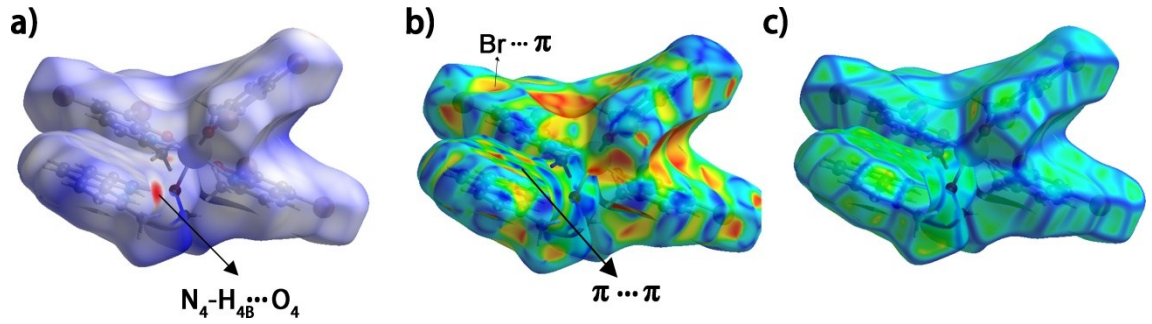

Figure S3. Hirshfeld surfaces mapped with d_{norm} (a) showing Shape-index (b) and Curvedness (c) for the **Br-1**.

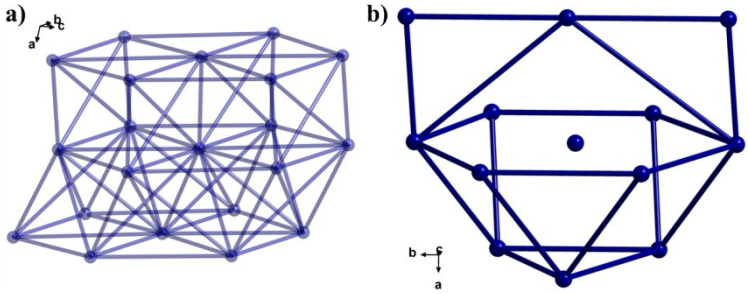

Figure S4. a) The connecting modes of the clusters through C–Cl/Br···π, π···π interactions and/or hydrogen bonds for **Cl-1** and **Br-1**; b) schematic view of the one *fcu* lattice net.

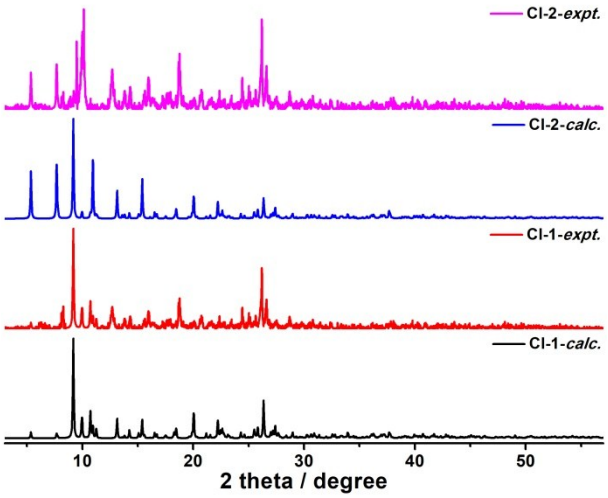

Figure S5a. The PXRD data for **Cl-1** and **Cl-2**.

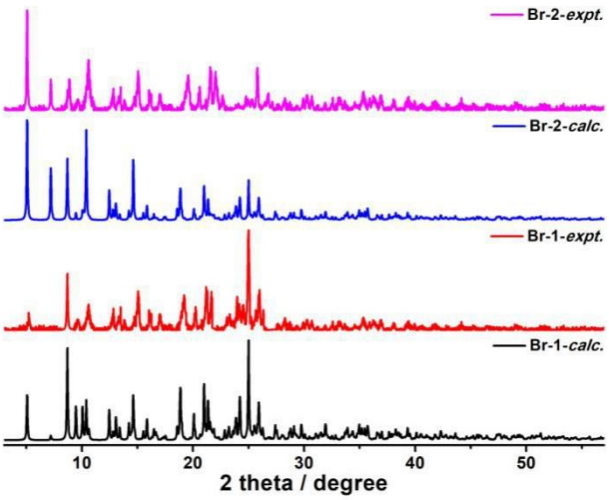

Figure S5b. The PXRD data for **Br-1** and **Br-2**.

Table S7a. Major species assigned in the HRESI-MS of **Cl-1**, **Cl-2**, **Br-1** and **Br-2** in positive mode.

Cl-1			
Peaks	Relative Intensity	*Obs. m/z*	*Calc. m/z*
$[Phen+H]^+$	0.782	209.11	209.11
$[Dy(L^1)_2(DMF)_2]^+$	1	761.99	762.00
$[Dy(L^1)_2(DMF)_3]^+$	0.274	835.05	835.05
$[Dy_2(L^1)_5(DMF)]^+$	0.067	1532.83	1532.82
Cl-2			
$[Dy(L^1)_2(DMF)_2]^+$	1	761.99	762.00
$[Dy(L^1)_2(DMF)_3]^+$	0.204	835.05	835.05
$[Dy_2(L^1)_5(DMF)]^+$	0.052	1532.83	1532.82
Br-1			
$[Phen+H]^+$	0.830	209.11	209.11
$[Dy(L^2)_2(DMF)_2]^+$	1	941.79	941.79
$[Dy(L^2)_2(DMF)_3]^+$	0.408	1014.84	1014.85
$[Dy_2(L^2)_4(CH_3O)(DMF)]^+$	0.034	1693.44	1693.45
Br-2			
$[Dy(L^2)_2(DMF)_2]^+$	1	941.79	941.79
$[Dy(L^2)_2(DMF)_3]^+$	0.311	1014.84	1014.85
$[Dy_2(L^2)_4(CH_3O)(DMF)]^+$	0.032	1693.44	1693.45

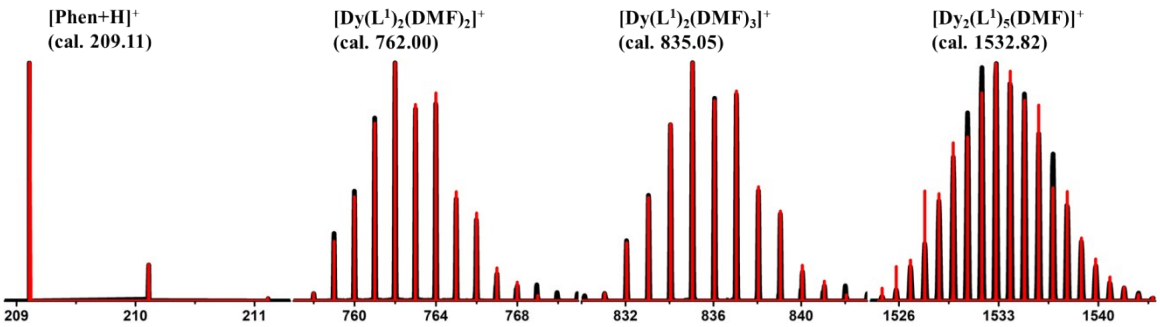

Figure S5c. The superposed simulated and observed spectra of several species for **Cl-1**.

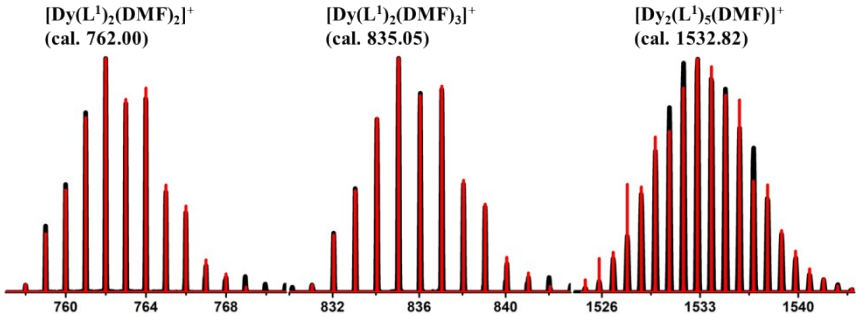

Figure S5d. The superposed simulated and observed spectra of several species for **Cl-2**.

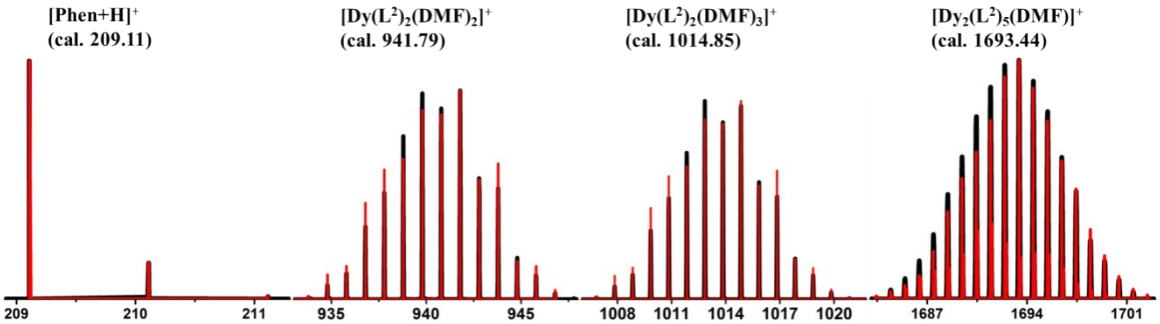

Figure S5e. The superposed simulated and observed spectra of several species for **Br-1**.

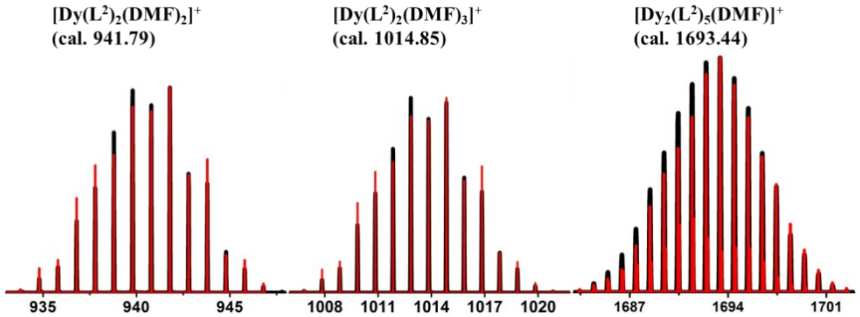

Figure S5f. The superposed simulated and observed spectra of several species for **Br-2**.

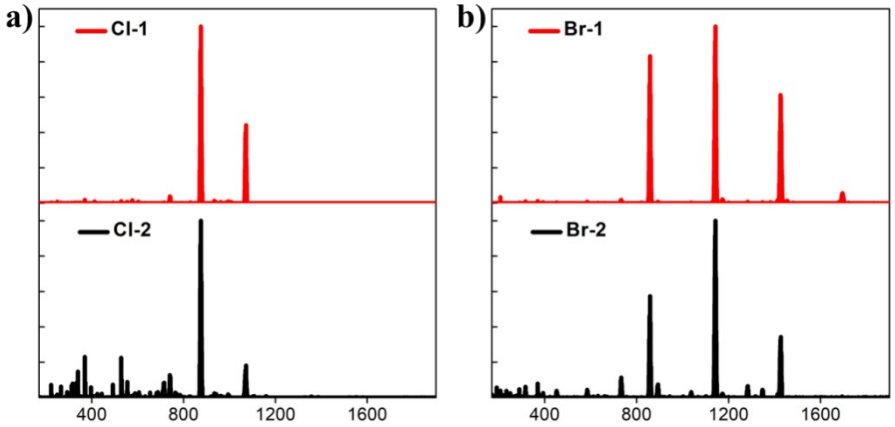

Figure S5g. HRESI-MS of a series of Dy-HOFs in negative mode: **Cl-1** (top in a), **Cl-2** (bottom in a), **Br-1** (top in b), and **Br-2** (bottom in b).

Table S7b. Major species assigned in the HRESI-MS of **Cl-1**, **Cl-2**, **Br-1** and **Br-2** in positive mode.

Cl-1			
Peaks	Relative Intensity	*Obs. m/z*	*Calc. m/z*
$[Dy(L^1)_3(CH_3O)]^-$	1	874.89	874.89
$[Dy(L^1)_4]^-$	0.441	1071.86	1071.85
Cl-2			
$[Dy(L^1)_3(CH_3O)]^-$	1	874.89	874.89
$[Dy(L^1)_4]^-$	0.180	1071.86	1071.85
Br-1			
$[Dy(L^2)_2(CH_3O)_2]^-$	0.832	857.72	857.73
$[Dy(L^2)_3(CH_3O)]^-$	1	1142.59	1142.59
$[Dy(L^2)_4]^-$	0.612	1427.43	1427.45
Br-2			
$[Dy(L^2)_2(CH_3O)_2]^-$	0.573	857.72	857.73
$[Dy(L^2)_3(CH_3O)]^-$	1	1142.59	1142.59
$[Dy(L^2)_4]^-$	0.342	1427.43	1427.45

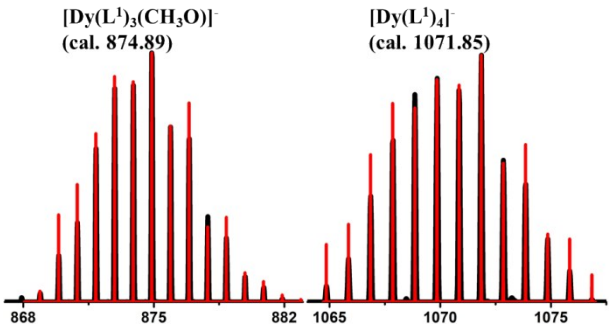

Figure S5h. The superposed simulated and observed spectra of several species for **Cl-1**.

Figure S5i. The superposed simulated and observed spectra of several species for **Cl-2**.

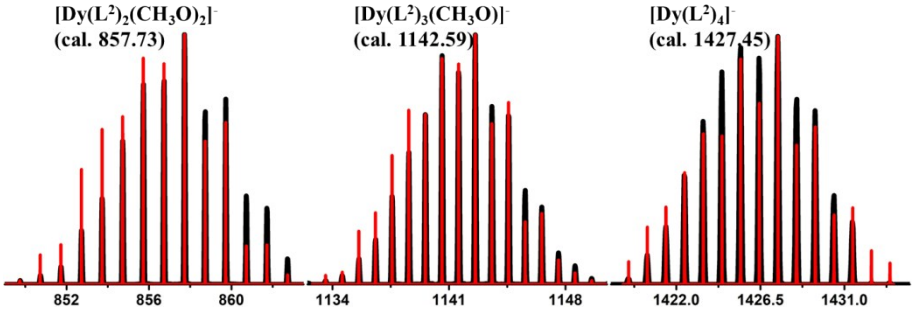

Figure S5j. The superposed simulated and observed spectra of several species for **Br-1** and **Br-2**.

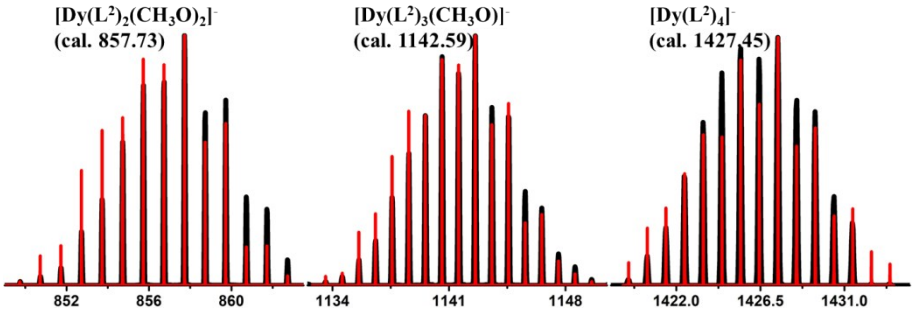

Figure S5k. The superposed simulated and observed spectra of several species for **Br-2**.

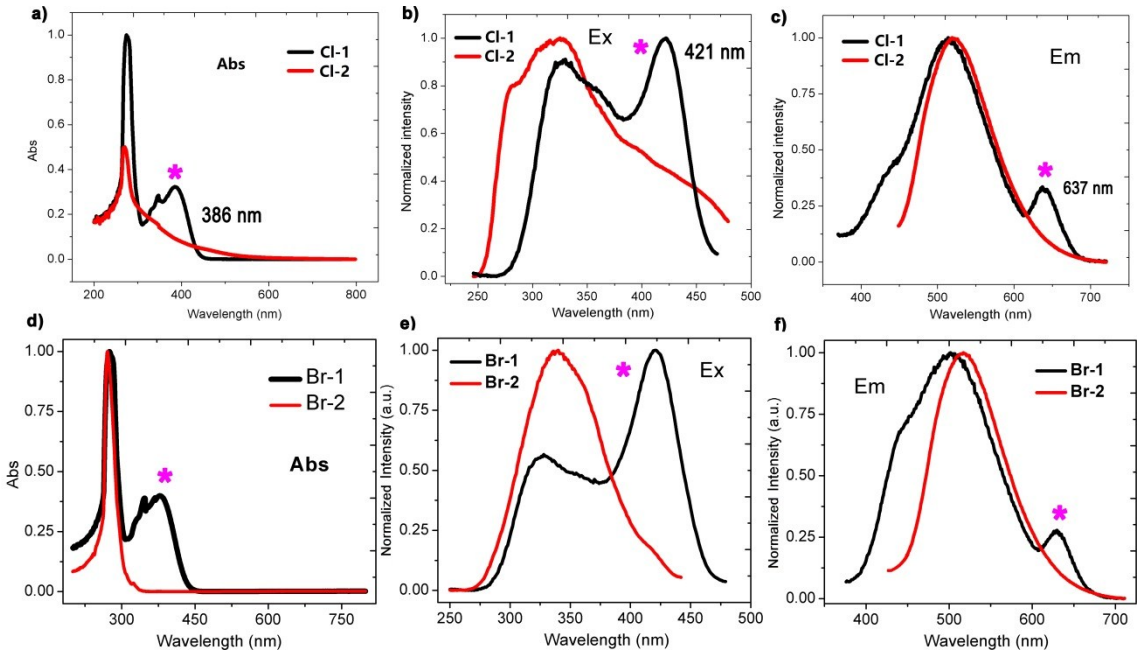

Figure S6. Ultraviolet-visible absorption spectrum (a/d) and fluorescence spectrum (b/e and c/f) of **Cl-1/Br-1** and **Cl-2/Br-2**.

The magnetic susceptibilities of **Cl-3** and **Br-3** were measured on direct-current field of 1000 Oe upon cooling from 300 to 2 K (Figure S7). The values of $\chi_m T$ were 14.09 $cm^3 \cdot K \cdot mol^{-1}$ for **Cl-3** (Figure S7a), and 13.88 $cm^3 \cdot K \cdot mol^{-1}$ for **Br-3** (Figure S7b) at room temperature, which were lower than the expected value of 14.17 $cm^3 \cdot K \cdot mol^{-1}$ for one uncorrelated Dy(III) ion ($^6H_{15/2}$, g = 4/3).[5] When the sample was cooled, $\chi_m T$ decreased marginally up to *ca.* 100 K before undergoing shallow minima at approximately 50 K. As the temperature decreased, the $\chi_m T$ values remained constant down to 50 K and then rapidly decrease to 7.76 $cm^3 \cdot K \cdot mol^{-1}$ for **Cl-3** (Figure S7a) and 10.63 $cm^3 \cdot K \cdot mol^{-1}$ for **Br-3** (Figure S7b) at 2 K, indicating the progressive depopulation of the excited stark sublevels of Dy(III) ions and/or weak inter-molecular magnetic interactions. [6,7] All the Dy-HOFs were further studied by micro-SQUID technique (Figure S8a). The M vs. H curves (Figure S8b) increased steeply at the crossing field H = 5 T.

The ac-susceptibilities were studied through three sets of measurements as a function of temperature for a range of frequencies spanning 10−1000 Hz by using an oscillating field of 2.5 Oe in 0 and 2000 Oe bias dc−field for **Cl-3** and **Br-3**. **Cl-3** showed not obviously slow relaxation behavior for out-of-phase (Figure S11a and S11b), but **Br-3** exhibited non-linear magnetization, *i.e.* non-zero out-of-phase susceptibility (χ''). The non-linearity appeared below more than 10 K for all frequencies in the range 1−1000 Hz (Figure S11c and S11d). There was a continuous trend of the ac-susceptibilities towards high temperature with increasing frequency. Therefore, after grinding, the main frame and the π–π interaction is destroyed or not as well by the mechanical force, but for **Cl-1**, the weak interaction was too strong, and the weak interaction of mechanical force damage was not evident, thus affecting the change of χ'' in zero field was not evident. However, the mechanical force of complex **Br-1** obviously destroyed more weak interaction bonds, which led to the obvious change of χ'' in zero field.[8]

The Cole–Cole plots followed a single-relaxation Debye model for **Br-3** (Figure S12). The fitting parameters τ (relaxation time) and α (width of the distribution of relaxation times) are listed in Table S10. α occurred at the range of 0.51–0.78, suggesting a narrow-to-moderate distribution of magnetic relaxation. Temperature dependent relaxation time was analyzed assuming a thermally activated process following Arrhenius law ($\tau = \tau_0 \exp(U_{eff}/k_B T)$). The energy barriers and extrapolated relaxation times were U_{eff} = 1.65 K and $\tau_0 = 1.2 \times 10^{-4}$ s

under zero dc field (Figure S13). And the energy barriers and extrapolated relaxation times were U_{eff} = 12.5 K and $\tau_0 = 1.5 \times 10^{-7}$ s under 2000 Oe dc field (Figure S13).

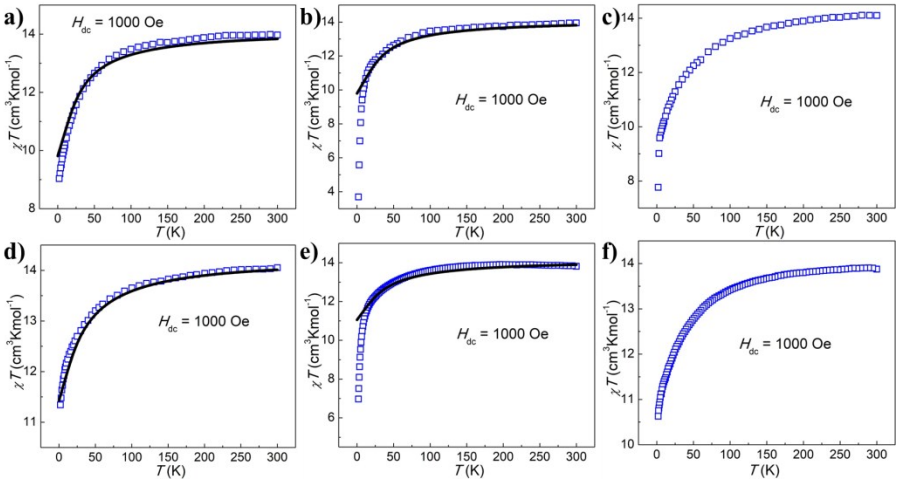

Figure S7. Temperature dependence of $\chi_m T$ for **Cl-1** (a), **Cl-2** (b), **Cl-3** (c), **Br-1** (d), **Br-2** (e) and **Br-3** (f).

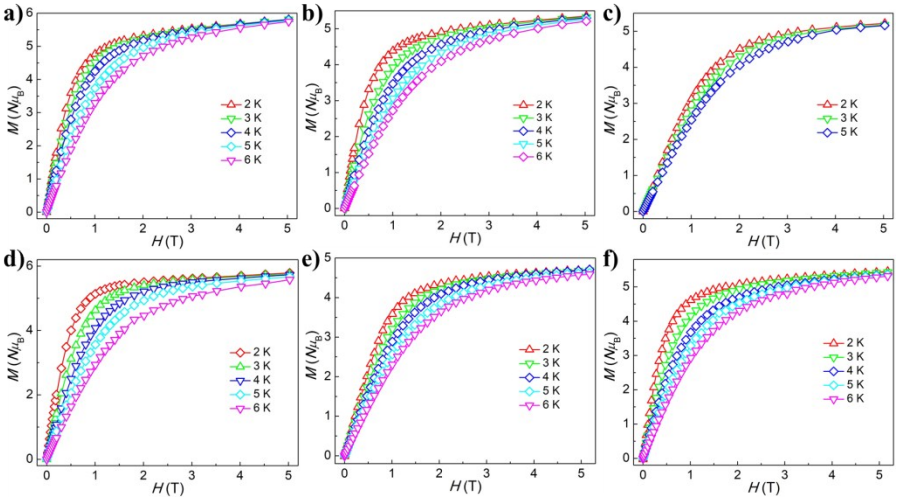

Figure S8a. Field dependence of the magnetization for **Cl-1**, **Cl-2**, **Cl-3** (a-c) and **Br-1**, **Br-2**, **Br-3** (d-f) at 2-6 K.

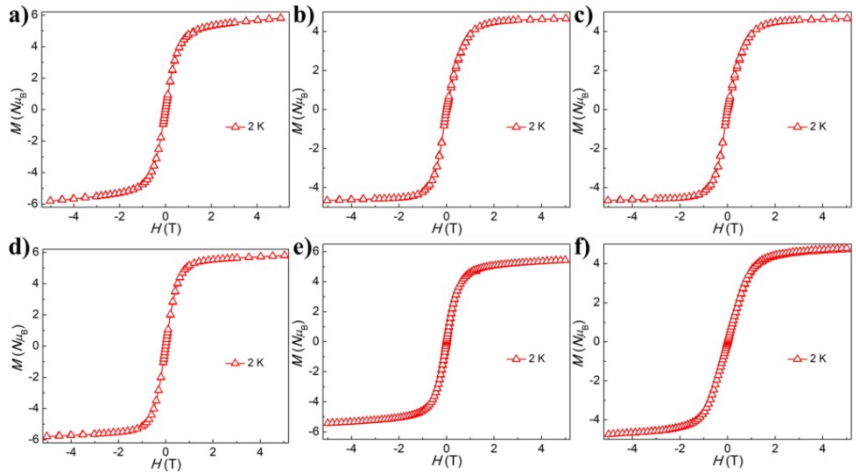

Figure S8b. The *M* vs. *H* curves for **Cl-1** (a), **Cl-2** (b), **Cl-3** (c) and **Br-1** (d), **Br-2** (e), **Br-3** (f) at 2 K.

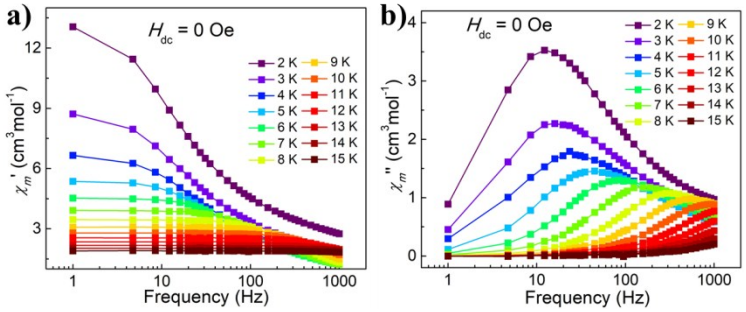

Figure S9. Variable-frequency dependent ac susceptibilities under 0 Oe field for **Cl-2**.

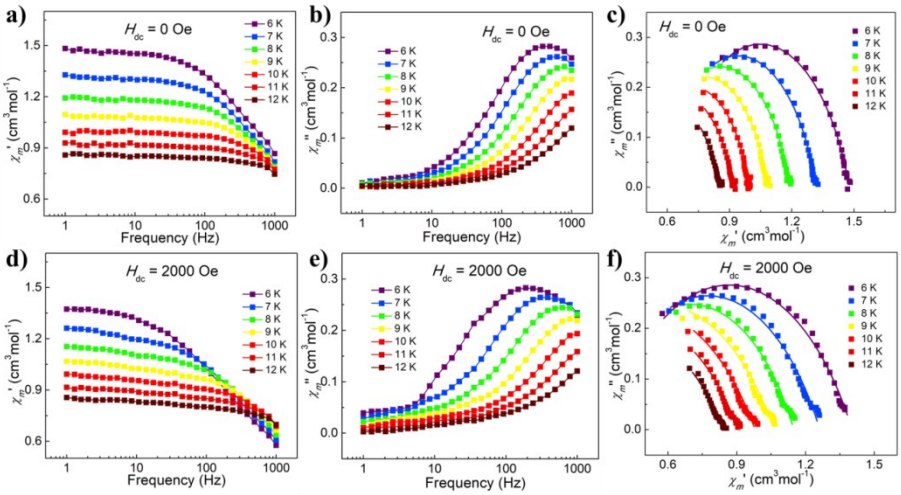

Figure S10a. Variable-frequency dependent ac susceptibilities and Cole-Cole plots from ac-susceptibilities for **Br-2** under 0 (a, b and c) and 2000 Oe (d, e and f) dc-field.

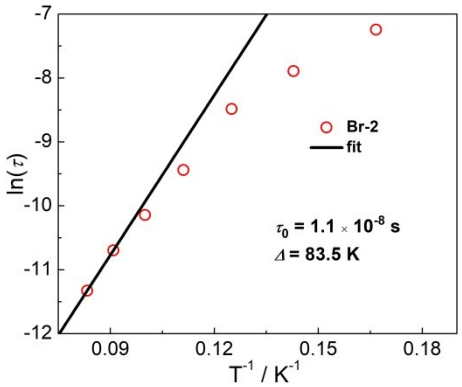

Figure S10b. Arrhenius plots generated from the temperature-dependent relaxation times extracted from the ac-susceptibilities Cole-Cole fits for **Br-2** in H_{dc} = 2000 Oe. The symbols and lines represent the extracted times and least-square fits.

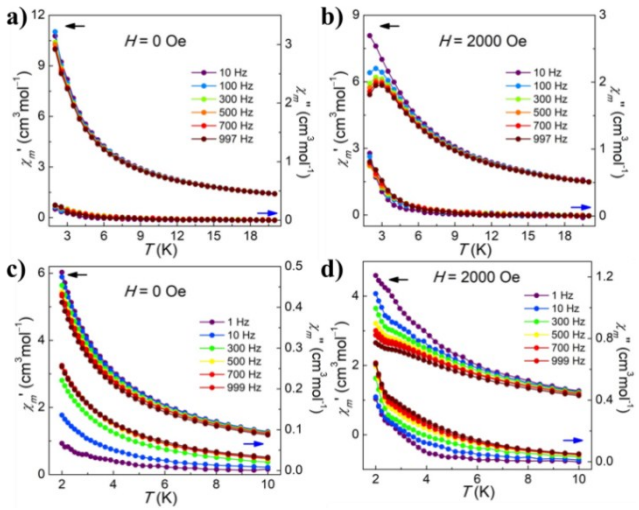

Figure S11. The temperature dependence of the in-phase (χ') and out-of-phase (χ'') ac-susceptibilities for different frequencies in 0 and 2000 Oe dc-field for **Cl-3** (a and b) and **Br-3** (c and d).

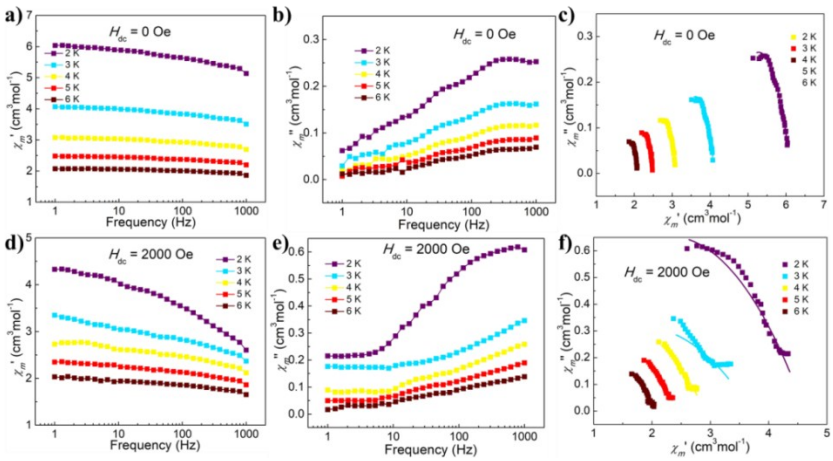

Figure S12. Variable-frequency dependent ac susceptibilities and Cole-Cole plots from ac-susceptibilities for **Br-3** under 0 and 2000 Oe dc-field.

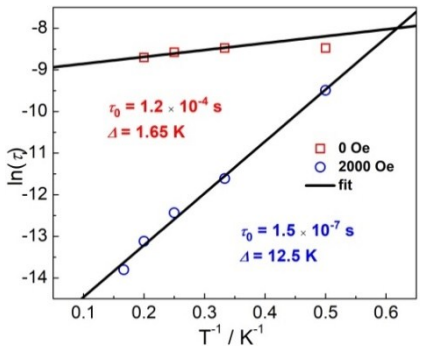

Figure S13. Arrhenius plots generated from the temperature-dependent relaxation times extracted from the ac-susceptibilities Cole-Cole fits for **Br-3** in H_{dc} = 0 Oe and H_{dc} = 2000 Oe, The symbols and lines represent the extracted times and least-square fits.

Table S8. Selected parameters from the fitting results of the Cole-Cole plots for **Cl-2** under 0 Oe dc-field.

	H_{dc}=0 Oe		
T (K)	*τ*	*α*	residual
2	1.07E-02	3.66E-01	1.59E+00
3	7.45E-03	3.78E-01	6.51E-01
4	4.98E-03	3.65E-01	3.26E-01
5	2.87E-03	2.99E-01	2.20E-01
6	1.54E-03	2.32E-01	1.28E-01
7	8.28E-04	1.71E-01	6.61E-02
8	4.71E-04	1.27E-01	2.80E-02
9	2.86E-04	9.55E-02	9.94E-03
10	1.81E-04	7.22E-02	2.42E-03
11	1.20E-04	5.79E-02	4.42E-03
12	7.81E-05	6.33E-02	2.51E-03
13	5.19E-05	6.75E-02	1.04E-03
14	2.57E-05	1.08E-01	2.09E-03
15	1.61E-05	1.12E-01	4.19E-03

Table S9. Selected parameters from the fitting results of the Cole-Cole plots for **Br-2** under 0 and 2000 Oe field.

	H_{dc}=0 Oe			H_{dc}=2000 Oe		
T (K)	*τ*	*α*	residual	*τ*	*α*	residual
6	3.65E-04	2.49E-01	1.75E-03	7.14E-04	3.77E-01	3.53E-03
7	2.84E-04	2.21E-01	1.09E-03	3.73E-04	3.68E-01	3.27E-03
8	2.12E-04	2.01E-01	9.09E-04	2.06E-04	3.61E-01	3.58E-03
9	1.52E-04	1.91E-01	8.10E-04	7.96E-05	4.12E-01	4.52E-03
10	1.06E-04	1.91E-01	9.92E-04	3.94E-05	4.28E-01	3.81E-03
11	6.17E-05	2.28E-01	1.11E-03	2.26E-05	4.36E-01	2.38E-03
12	2.47E-05	2.97E-01	8.23E-04	1.20E-05	4.62E-01	1.43E-03

Table S10. Selected parameters from the fitting results of the Cole-Cole plots for **Br-3** under 0 and 2000 Oe field.

	H_{dc}=0 Oe			H_{dc}=2000 Oe		
T (K)	*τ*	*α*	residual	*τ*	*α*	residual
2	2.08E-04	6.20E-01	1.55E-02	7.55E-05	6.49E-01	3.84E-02
3	2.08E-04	5.92E-01	7.67E-03	9.05E-06	7.87E-01	4.99E-02
4	1.88E-04	5.74E-01	4.92E-03	3.98E-06	7.25E-01	1.84E-02
5	1.66E-04	5.65E-01	3.32E-03	2.01E-06	7.23E-01	5.02E-03
6	2.04E-04	5.10E-01	2.54E-03	1.01E-06	7.21E-01	6.93E-03

Computational details

Complete-active-space self-consistent field (CASSCF) calculations on four complexes (see Figure S14a for the four calculated model structures) on the basis of single-crystal X-ray determined geometries have been carried

out with MOLCAS 8.2 program package.[9] The basis sets for all atoms are atomic natural orbitals from the MOLCAS ANO-RCC library: ANO-RCC-VTZP for Dy^{III} ion; VTZ for close O and N; VDZ for distant atoms. The calculations employed the second order Douglas-Kroll-Hess Hamiltonian, where scalar relativistic contractions were taken into account in the basis set and the spin-orbit couplings were handled separately in the restricted active space state interaction (RASSI-SO) procedure. For all complexes, active electrons in 7 active spaces include all *f* electrons (CAS(9 in 7)) in the CASSCF calculation. To exclude all the doubts, we calculated all the roots in the active space. We have mixed the maximum number of spin-free state which was possible with our hardware (all from 21 sextets, 128 from 224 quadruplets, 130 from 490 doublets). SINGLE_ANISO[10] program was used to obtain energy levels, ***g*** tensors, m_J values, magnetic axes, *et al.,* based on the above CASSCF/RASSI-SO calculations.

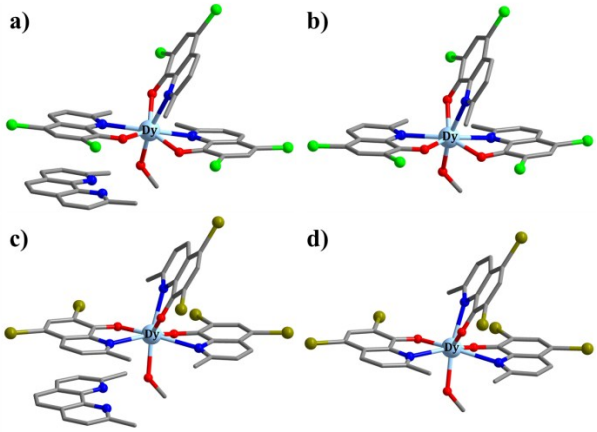

Figure S14a. Calculated structures of four models— **Cl-1** (a), **Cl-2** (b), **Br-1** (c), **Br-2** (d); H atoms are omitted.

Table S11a. Calculated energy levels (cm^{-1}), ***g*** (g_x, g_y, g_z) tensors and predominant m_J values of the lowest eight Kramers doublets (KDs) of four models using CASSCF/RASSI-SO with MOLCAS 8.2.

KDs	**Cl-1**						**Br-1**					
	Cl-1			**Cl-2**			**Br-1**			**Br-2**		
	E	***g***	m_J	*E*	***g***	m_J	*E*	***g***	m_J	*E*	***g***	m_J
1	0.0	0.505 1.823 17.614	±15/2	0.0	0.516 1.845 17.596	±15/2	0.0	0.280 0.721 19.019	±15/2	0.0	0.324 0.908 18.783	±15/2
2	60.9	0.216 1.508 14.892	±13/2	71.8	0.655 1.747 14.234	±13/2	60.5	1.014 1.370 16.592	±13/2	69.7	1.353 1.640 15.768	±13/2
3	165.9	4.049 6.167 10.614	±9/2	190.3	8.620 7.498 4.493	±9/2	142.6	4.100 5.774 9.935	±9/2	158.4	4.281 6.279 9.296	±9/2
4	237.2	1.284 3.418 10.006	±1/2	275.4	0.054 1.495 10.405	±3/2	220.6	1.402 4.068 9.040	±7/2	243.4	0.829 2.996 9.416	±7/2
5	336.0	0.534 0.960 14.100	±5/2	391.8	0.372 0.946 13.224	±5/2	327.7	0.743 1.636 12.222	±3/2	359.7	0.683 1.436 12.010	±3/2
		0.410			0.437			0.698			0.048	

6	457.8	0.750 17.250	±3/2	518.4	0.619 15.296	±1/2	424.4	0.894 13.759	±1/2	465.8	0.621 14.065	±1/2
7	506.4	0.276 1.061 18.447	±7/2	577.0	0.339 0.897 17.341	±7/2	456.6	0.354 1.500 16.930	±5/2	520.4	0.197 0.571 17.364	±5/2
8	576.0	0.022 0.038 19.625	±11/2	638.0	0.044 0.054 19.257	±11/2	583.7	0.007 0.010 19.800	±11/2	628.2	0.009 0.012 19.742	±11/2

Table S11b. In wave functions with definite projection of the total moment | *JM* > for the lowest two KDs for four models using CASSCF/RASSI-SO with MOLCAS 8.2.

	E	wave functions
Cl-1	0.0	68.31%|±15/2>+25.58%|±11/2>
	60.9	68.42%|±13/2>+15.50%|±9/2>+7.05%|±11/2>
Cl-2	0.0	68.60%|±15/2>+24.91%|±11/2>
	71.8	64.47%|±13/2>+20.52%|±9/2>+5.08%|±5/2>
Br-1	0.0	88.89%|±15/2>+7.46%|±11/2>
	60.5	43.66%|±13/2>+14.29%|±11/2>24.34%|±9/2>5.89%|±7/2>
Br-2	0.0	85.88%|±15/2>+9.42%|±11/2>
	69.7	45.41%|±13/2>+9.80%|±11/2>+23.87%|±9/2>+5.52%|±7/2>+6.82%|±5/2>
Br2-2	0.0	98.57%|±15/2>
	194.8	92.39%|±13/2>

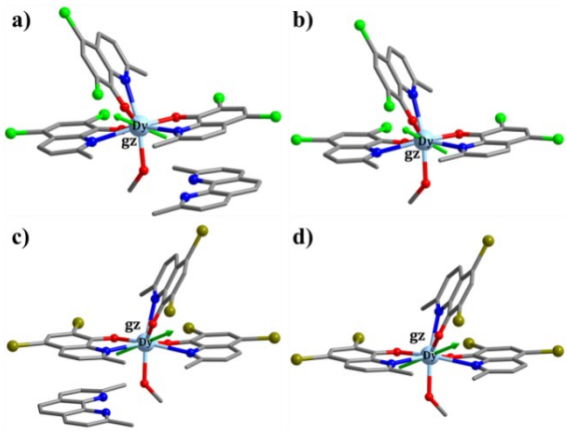

Figure S14b. Calculated orientations of the local main magnetic axes of the ground KDs on Dy^{III} ion of four models— **Cl-1** (a), **Cl-2** (b), **Br-1** (c), **Br-2** (d).

The X-ray diffraction result suggested that **Br2-1** crystallized in the monoclinic crystal system with the $P2_1/n$ space group (Table S2a), in which the nine-coordinated Dy(III) core was surrounded by one nitrogen atom and one oxygen atom from one 5,7-dibromo-2-methyl-8-quinolinol ligand, six oxygen atoms from three nitrate anions and one oxygen atom from one methanol (Table S2b). **Br2-1** was found to be mononuclear cluster consisting of two

free Phen organic molecules and one protonated Phen, those free organic molecules not only influenced intermolecular weak interaction, but also affected intermolecular stacking (Figure S15). The Dy-N bond distance was 2.538 Å and the Dy-O distance was 2.213 Å between Dy(III) ion and ligand, the Dy-O bond distance between Dy(III) ion and methanol was 2.339 Å, and the bond distances fell in range of 2.429-2.513 Å between Dy(III) ion and nitrate anions (Table S2b). Based *SHAPE* analysis, the calculated result suggested that the nine coordinated Dy^{III} cores could be viewed as a muffin geometry (Table S12a).[11] The supramolecular weak action of **Br2-1** structure contained C-H···O, O-H···N, N-H···O and π···π, respectively, which bond distances were N-H···O (1.840 Å), C-H···O (2.453 ~ 2.562 Å), N-H···O (2.004 Å) and π···π (3.456, 3.574, 3.741 and 3.742 Å) (Figure S15a, S15b, Table S12b). The supramolecular weak action distances were all within a reasonable range and could thus be considered to form 14-connected ***fcu*** net with distances of 9.592-14.674 Å between the centers of the Dy-HOFs (Figure S15a(e)).[12]

Table S12a. *SHAPE* analysis of the Dy^{III} ion in **Br2-1**.

Label	Shape	Symmetry	Distortion(°)
EP-9	D_{9h}	Enneagon	35.607
OPY-9	C_{8v}	Octagonal pyramid	23.464
HBPY-9	D_{7h}	Heptagonal bipyramid	16.375
JTC-9	C_{3v}	Johnson triangular cupola J3	16.196
JCCU-9	C_{4v}	Capped cube J8	7.502
CCU-9	C_{4v}	Spherical-relaxed capped cube	6.181
JCSAPR-9	C_{4v}	Capped square antiprism J10	5.469
CSAPR-9	C_{4v}	Spherical capped square antiprism	3.915
JTCTPR-9	D_{3h}	Tricapped trigonal prism J51	6.071
TCTPR-9	D_{3h}	Spherical tricapped trigonal prism	4.466
JTDIC-9	C_{3v}	Tridiminished icosahedron J63	11.592
HH-9	C_{2v}	Hula-hoop	8.652
MFF-9	C_s	Muffin	2.754

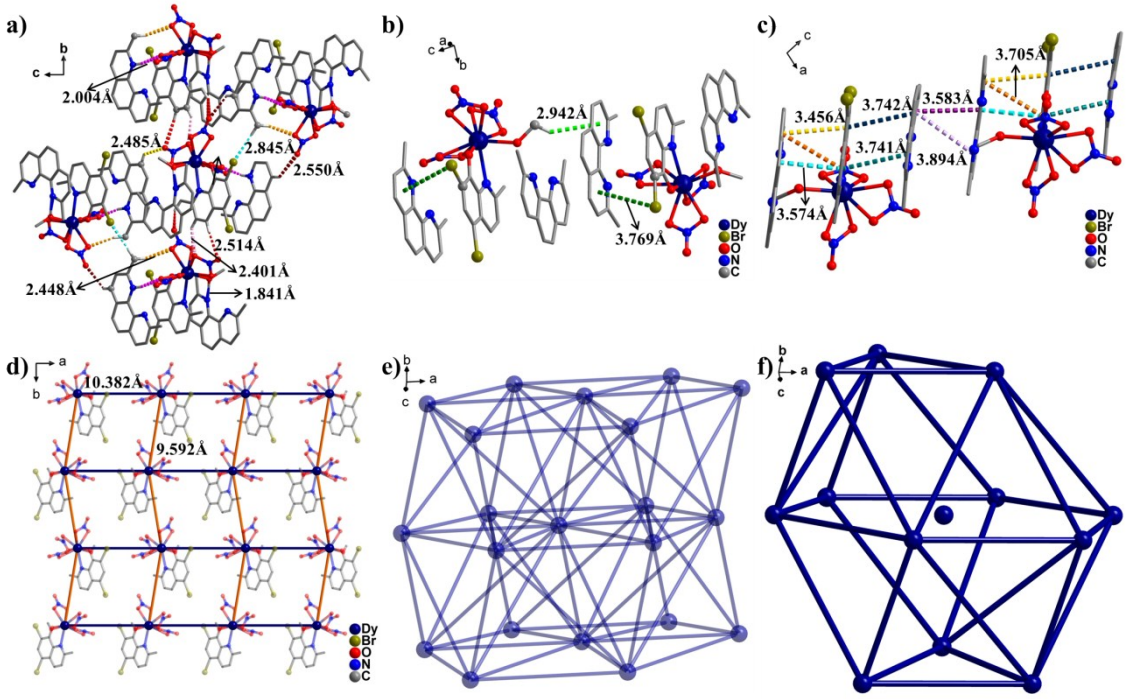

Figure S15a. Intermolecular interactions in the structure of **Br2-1**. (a) N_8-H_8···O_2 (pink dotted line) O_{13}-H_{13}···N_5 (blue dotted line), C-H···O (red, gold, rose, light orange or dark red dotted line), and C_{37}-H_{37B}···Br_2 (turquoise dotted line); (b) C_8-Br_2···π(PhC_5N) (green dotted line) and C_{11}-H_{11A}···π(PhC_5N) (bright green dotted line); (c) π(Ph or PhC_5N)···π(Ph or PhC_5N) (orange, aqua, gold, teal, lavender, violet or dark teal dotted line) ; (d) connecting cluster to cluster (orange, dark blue line); e) the connecting modes of the clusters through C–Br···π, π···π interactions and/or hydrogen bonds for **Br2-1**; f) schematic view of the one *fcu* lattice net.

Table S12b. Hydrogen-bond and C-H···π bonds geometries and π···π interactions for **Br2-1**.

Hydrogen bond	**Distance[a], Å**	**Angle[b], °**
N_8-H_8···O_2	2.004	162
O_{13}-H_{13}···N_5	1.840	169
C_4-H_4···O_9	2.510	152
C_{12}-H_{12A}···O_1	2.562	150
C_{14}-H_{14}···O_4	2.496	152
C_{37}-H_{37C}···O_{10}	2.453	144
π···π	**Distance[c], Å**	**Distance[d], Å**
π(PhC_5N)··· π(PhC_5N)	3.705(3)	3.373(2)
π(Ph)··· π(PhC_5N)	3.574(3)	3.303(3)
π(Ph)··· π(PhC_5N)	3.456(3)	3.360(2)
π(PhC_5N)··· π(PhC_5N)	3.741(4)	3.463(2)
π(PhC_5N)··· π(PhC_5N)	3.894(3)	3.338(2)
π(Ph)··· π(PhC_5N)	3.582(3)	3.328(3)
π(Ph)··· π(Ph)	3.742(4)	3.433(2)
C–X···π	**Distance[c], Å**	**Angle[e], °**
C_{11}-H_{11A}···π(PhC_5N)	2.942	146

[a]Distance between acceptor and donor; [b]Angle of acceptor–hydrogen–donor; [c]Centroid–to–centroid distance; [d] Interplanar distance; [e]Angle of carbon–hydrogen–centroid.

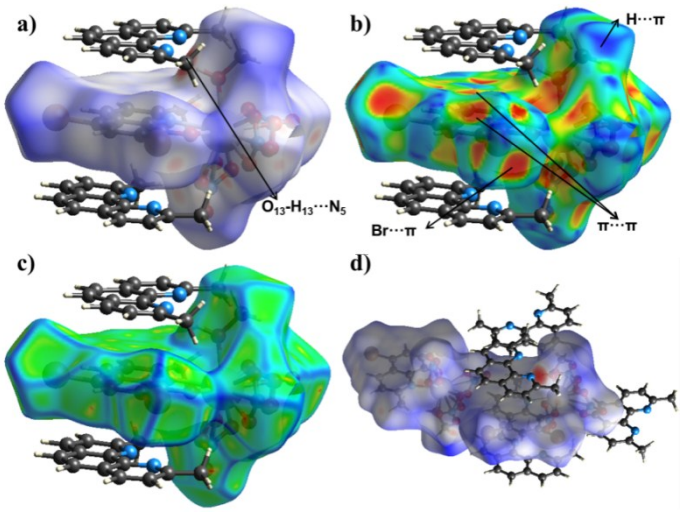

Figure S15b. Hirshfeld surfaces mapped with d_{norm} (a and d) showing Shape-index (b) and Curvedness (c) for the **Br2-1**.

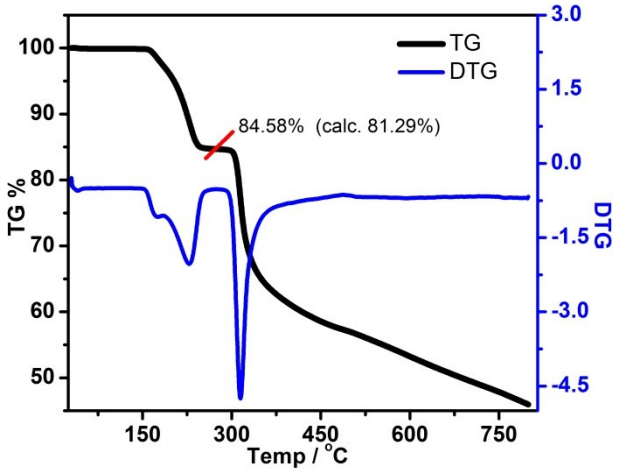

Figure S16a. Thermogravimetry of **Br2-1** at a heating rate of 5 °C/min under N_2 atmosphere.

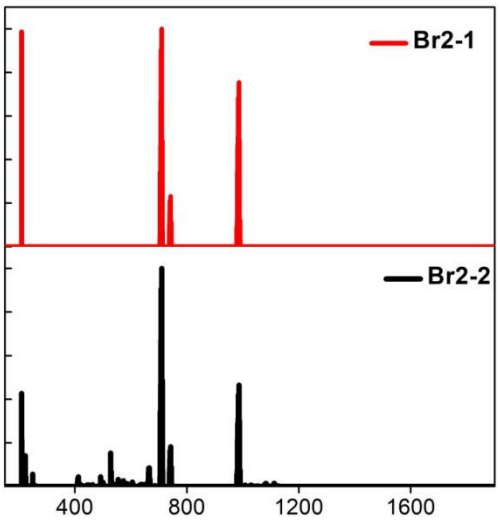

Figure S16b. HRESI-MS of **Br2-1** (top) and **Br2-2** (bottom) in positive mode.

Table S13a. Major species assigned in the HRESI-MS of **Br2-1** and **Br2-2** in positive mode.

Br2-1			
$[Phen+H]^+$	0.987	209.11	209.11
$[Dy(L^2)(NO_3)_2(CH_3OH)(DMF)]^+$	1	709.87	709.87
$[Dy(L^2)(NO_3)_2(CH_3OH)_2(DMF)]^+$	0.231	741.90	741.90
$[Dy(L^2)_2(NO_3)_2(CH_3OH)_2]^+$	0.754	985.73	985.73
Br2-2			
$[Phen+H]^+$	0.426	209.11	209.11
$[Dy(L^2)(NO_3)_2(CH_3OH)(DMF)]^+$	1	709.87	709.87
$[Dy(L^2)(NO_3)_2(CH_3OH)_2(DMF)]^+$	0.181	741.90	741.90
$[Dy(L^2)_2(NO_3)_2(CH_3OH)_2]^+$	0.465	985.73	985.73

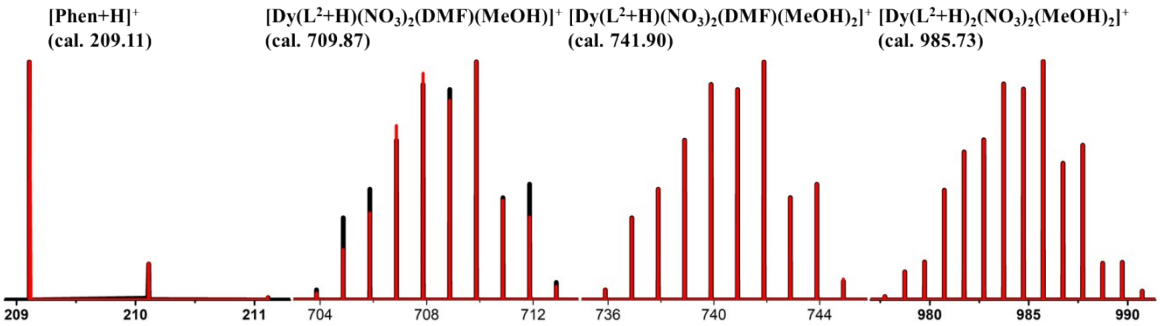

Figure S16c. The superposed simulated and observed spectra of several species for **Br2-1**.

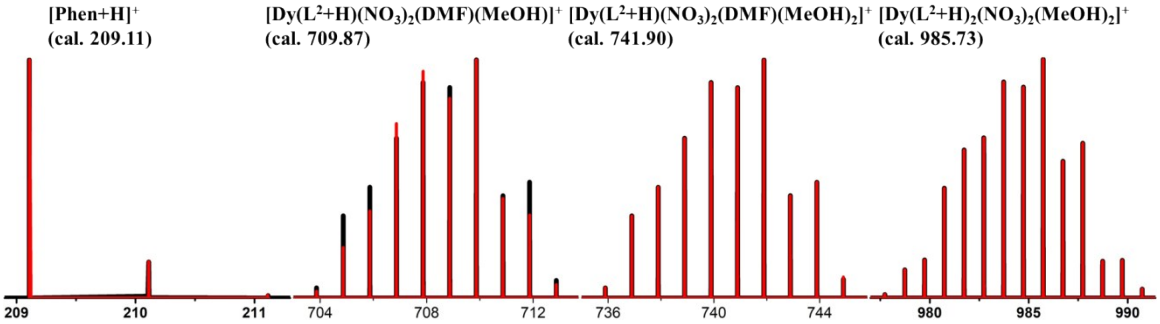

Figure S16d. The superposed simulated and observed spectra of several species for **Br2-2**.

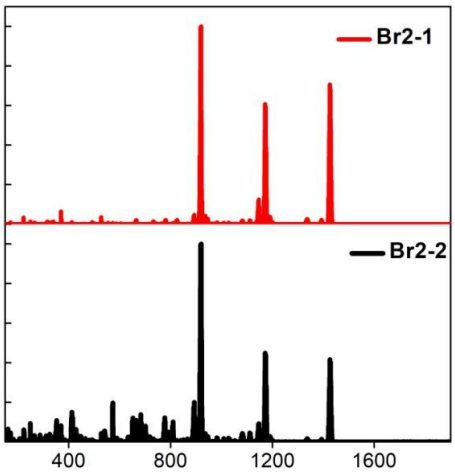

Figure S16e. HRESI-MS of **Br2-1** (top) and **Br2-2** (bottom) in negative mode.

Table S13b. Major species assigned in the HRESI-MS of **Br2-1** and **Br2-2** in negative mode.

Br2-1			
$[Dy(L^2)_2(NO_3)_2]^-$	1	919.67	919.66
$[Dy(L^2)_3(NO_3)]^-$	0.607	1173.55	1173.56
$[Dy(L^2)_4]^-$	0.681	1427.43	1427.45
Br2-2			
$[Dy(L^2)_2(NO_3)_2]^-$	1	919.67	919.66
$[Dy(L^2)_3(NO_3)^-$	0.449	1173.55	1173.56
$[Dy(L^2)_4]^-$	0.402	1427.43	1427.45

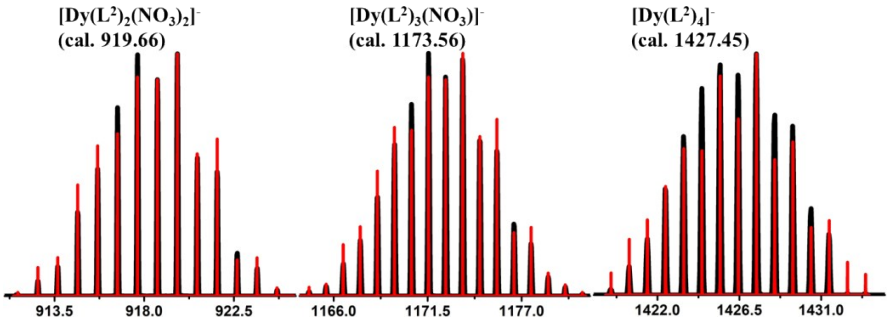

Figure S16f. The superposed simulated and observed spectra of several species for **Br2-1**.

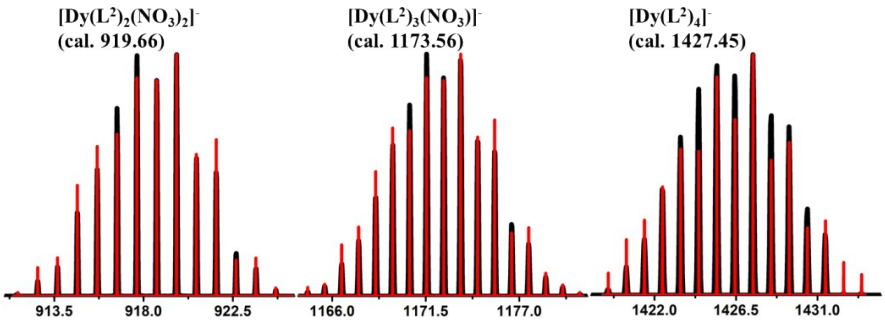

Figure S16g. The superposed simulated and observed spectra of several species for **Br2-2**.

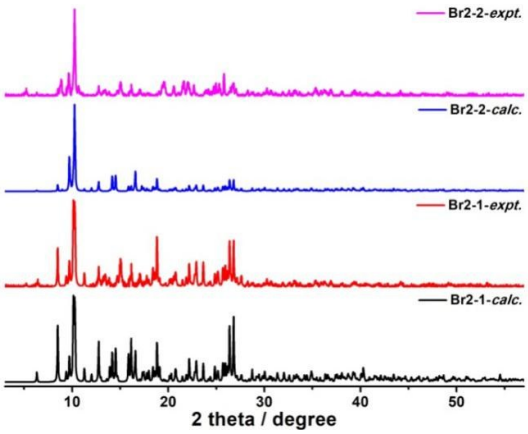

Figure S16h. The PXRD data for **Br2-1** and **Br2-2**.

The magnetic susceptibilities of polycrystalline samples of **Br2-1** were measured on dc field of 1000 Oe upon cooling from 300 to 2 K (Figure S17). The values of $\chi_m T$ were normal, which were slightly lower than the expected value of 14.17 $cm^3 \cdot K \cdot mol^{-1}$ for one uncorrelated Dy(III) ion ($^6H_{15/2}$, g = 4/3).[5] The non-superposition of M and H/T data were showed in Figure S18.

The ac-susceptibilities were studied through three sets of measuremeβts as a function of temperature for a range of frequencies spanning 10−1000 Hz by using an oscillating field of 2.5 Oe in the 0 and 2000 Oe bias dc−field for **Br2-1**, **Br2-2** and **Br2-3**. The analysis of magnetic data of Dy-HOFs **Br2-1** showed that it exhibited weak field-induced single-molecule-magnetic behavior (Figure S19a and S19d). When we kept **Br2-1** at 260 °C for 2 h, only Phen in the channel was removed to obtain **Br2-2**, and Phen+H could not remove. The ac-susceptibilities suggested that it was found that the single-molecule magnetic behavior of complex **Br2-2** was slightly more obvious, especially under high field. There was a very evident slow relaxation phenomenon which indicates that the mechanical force only destroyed a part of the weaker interaction and improved the single-molecule-magnetic behavior of the Dy-HOFs (Figure S19c, S19f). When we measured the ground samples **Br2-3**, the magnetic properties were only slightly improved (Figure S19b, S19e).[8]

The Cole-Cole plots (Figure S20-21 for **Br2-2** and **Br2-3**) followed a single relaxation Debye model. The fitting parameters τ (relaxation time) and α (α determines the width of the distribution of relaxation times) were listed in Table S14. The parameter α for **Br2-2** and **Br2-3** fell in the range of 0.46-0.63, suggesting a narrow-to-moderate distribution of magnetic relaxation. Temperature dependent relaxation time was analyzed assuming a thermally activated process following the Arrhenius law ($\tau = \tau_0 \exp(U_{eff}/k_B T)$). The energy barriers and extrapolated relaxation times were U_{eff} = 2.1 K and $\tau_0 = 1.5 \times 10^{-5}$ s for **Br2-2**, and U_{eff} = 5.2 K and $\tau_0 = 2.6 \times 10^{-5}$ s for **Br2-3** under zero dc field (Figure 20a(d)). Complete-active-space self-consistent field (CASSCF) calculations of three complexes on the basis of X-ray determined geometries have been carried out with MOLCAS 8.2[9] (see Supporting Information for details). SINGLE_ANISO[10] program was used to obtain the energy levels, ***g*** tensors, predominant m_J values, magnetic axes, *et al.,* based on the above CASSCF/RASSI-SO calculations. The calculated model structure of **Br2-2** is shown in Figure S21a. The lowest eight Kramers Doublets (KDs) (cm^{-1}), the corresponding ***g*** tensors and the predominant m_J values are shown in Table S15, where the energy gap between the lowest two KDs of **Br2-2** is much larger than those of **Cl-1** and **Br-1**. The m_J components for the lowest two KDs of five models are shown in Table S11b. In contrast, the ground KDs for **Br2-2** are all mostly composed by m_J =±15/2, resulting in a small transversal magnetic moment in its ground KDs shown in Figure S21c. The main magnetic axes on Dy^{III} ion is shown in Figure S21b. For **Br2-2**, the transversal magnetic moment is ca. 10^{-2} μ_B, therefore the QTM in its KDs is suppressed at low temperature. The calculated results show that the experimental values of **Br2-2** are quite different from the calculated values. It is found that **Br2-2** has abundant weak effects, which are not taken into

account in the calculation (Figure S21, Table S11b and S15).

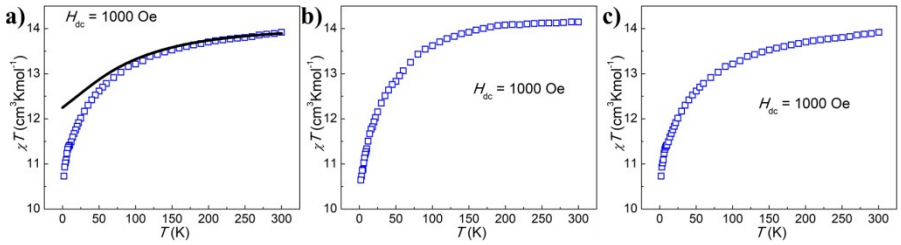

Figure S17. Temperature dependence of $\chi_m T$ for **Br2-1** (a), **Br2-2** (b) and **Br2-3** (c).

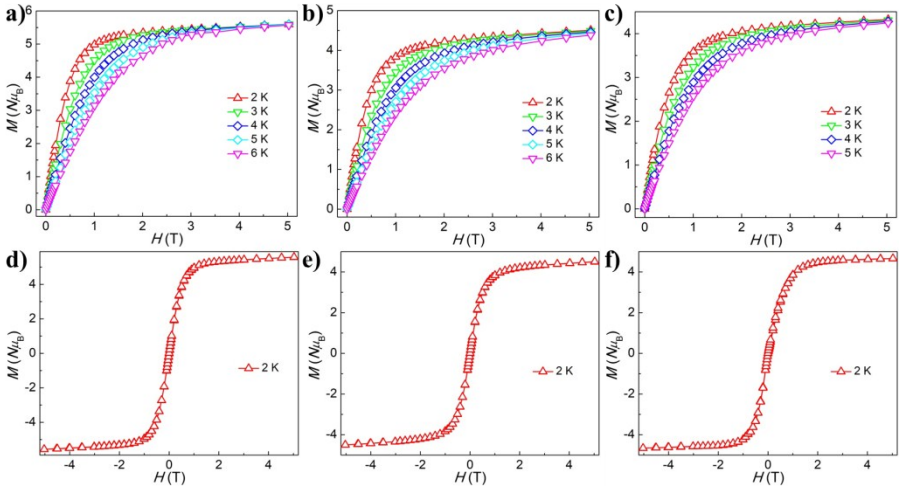

Figure S18. Field dependence of the magnetization for **Br2-1** (a), **Br2-2** (b) and **Br2-3** (c) at 2-6 K, and their *M* vs. *H* curves (d-f).

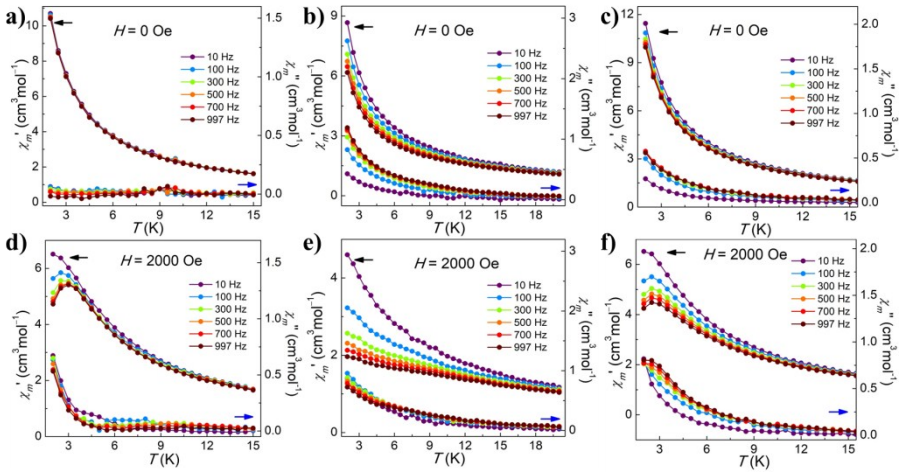

Figure S19. The temperature dependence of the in-phase (χ') and out-of-phase (χ'') ac-susceptibilities for different frequencies in 0 and 2000 Oe dc-field for **Br2-1** (a and d), **Br2-2** (c and f) and **Br2-3** (b and e).

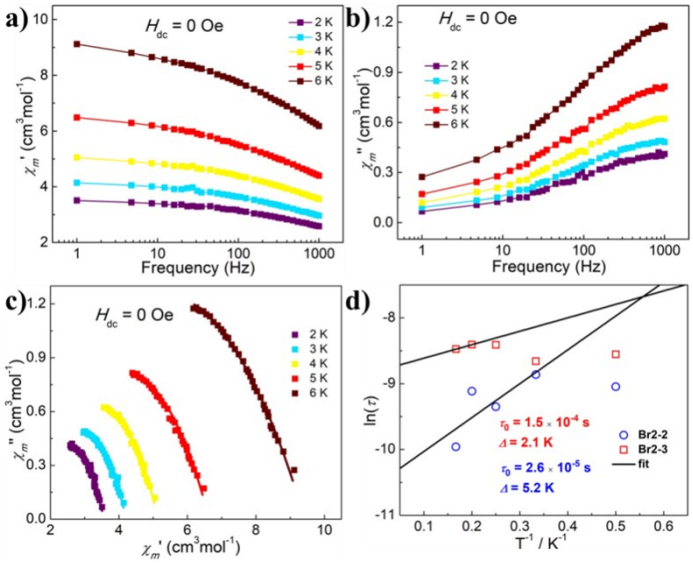

Figure S20a. Variable-frequency dependent ac susceptibilities and Cole-Cole plots from ac-susceptibilities for **Br2-2** (a, b and c) under 0 Oe dc-field, and Arrhenius plots generated from the temperature-dependent relaxation times extracted from the ac-susceptibilities Cole-Cole fits for **Br2-2** (d) and **Br2-3** (d).

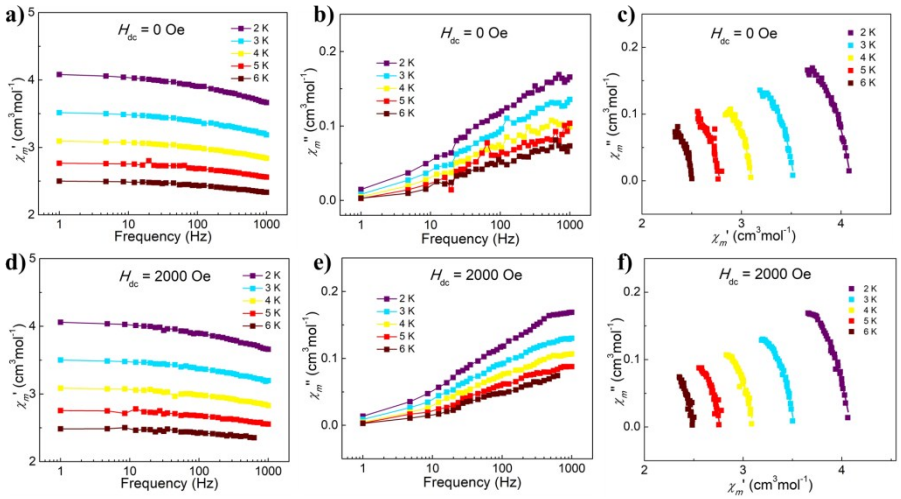

Figure S20b. Variable-frequency dependent ac susceptibilities and Cole-Cole plots from ac-susceptibilities for **Br2-3** under 0 dc-field (a and b) and 2000 Oe dc-field (d and e), and Arrhenius plots generated from the temperature dependent relaxation times extracted from the ac-susceptibilities Cole-Cole fits for **Br2-3** (c and f).

Table S14a. Selected parameters from the fitting results of the Cole-Cole plots for **Br2-2** under 2000 Oe field.

	Br2-2		
T (K)	*τ*	*α*	residual
2	1.18E-04	5.27E-01	9.99E-03
3	1.42E-04	5.41E-01	1.88E-02
4	8.70E-05	5.77E-01	8.93E-03
5	1.10E-04	5.90E-01	2.03E-02
6	4.72E-05	6.31E-01	1.42E-02

Table S14b. Selected parameters from the fitting results of the Cole-Cole plots for **Br2-3** under 2000 Oe field.

	0 Oe			2000 Oe		
T (K)	*τ*	*α*	residual	*τ*	*α*	residual
2	1.93E-04	5.14E-01	1.42E-03	1.05E-04	5.58E-01	2.34E-03
3	1.74E-04	5.13E-01	1.50E-03	2.35E-04	4.88E-01	9.13E-04
4	2.22E-04	4.85E-01	8.31E-04	1.21E-04	5.47E-01	4.38E-03
5	2.23E-04	4.61E-01	6.79E-03	3.02E-04	4.42E-01	4.62E-03
6	2.08E-04	4.73E-01	1.08E-03	1.57E-04	4.93E-01	3.13E-03

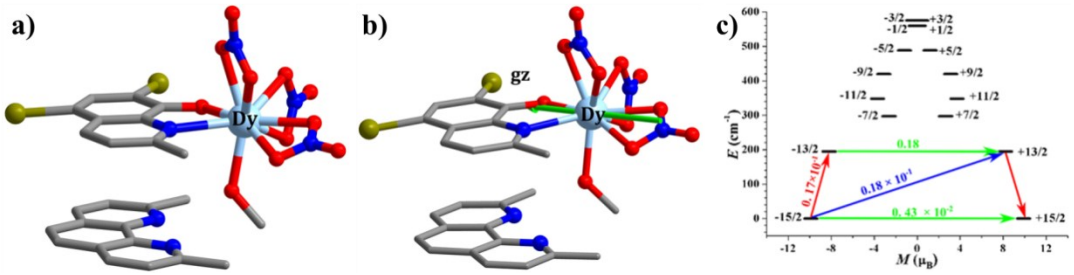

Figure S21. (a) Calculated structures of **Br2-2**; H atoms are omitted; (b) Calculated orientations of the local main magnetic axes of the ground KDs on DyIII ions of **Br2-2**; (c) The magnetization blocking barriers in **Br2-2**. The thick black lines represent the KDs as a function of their magnetic moments along the magnetic axis. The green lines correspond to diagonal quantum tunneling of magnetization (QTM); the blue lines represent Orbach relaxation process. The path shown by the red arrows represents the most possibly path for magnetic relaxation in the corresponding compounds. The numbers at each arrow stand for the mean absolute values of the transversal magnetic moments.

Table S15. Calculated energy levels (cm^{-1}), ***g*** (g_x, g_y, g_z) tensors and predominant m_J values of the lowest eight Kramers doublets (KDs) of five models using CASSCF/RASSI-SO with MOLCAS 8.2.

KDs		1	2	3	4	5	6	7	8
Br2-2	*E*	0.0	194.8	296.9	348.2	419.2	488.1	559.7	575.2
	g	0.012	0.404	2.705	7.772	8.540	1.820	0.220	0.102
		0.014	0.659	4.101	5.516	5.876	2.982	0.761	1.179
		19.793	16.497	13.833	2.520	3.010	13.207	17.184	17.125
	m_J	±15/2	±13/2	±7/2	±11/2	±9/2	±5/2	±1/2	±3/2

Dy-HOFs **Br3-1** crystallized in the monoclinic crystal system with the $P2_1/c$ space group (Table S2a and S2b), in which the seven-coordinated Dy(III) cores were surrounded by three nitrogen atoms and three oxygen atoms from three 5,7-dibromo-2-methyl-8-quinolinol ligands and one coordinated Cl^- ion. **Br3-1** was found to be mononuclear cluster consisting of a free 2-methylquinoline (L3) organic molecule for **Br3-1**. Similarly, this free organic molecule not only influenced intermolecular weak interaction, but also affected intermolecular stacking (Figure S22). The bond distances between Dy(III) ion and ligand nitrogen atoms fell in range of 2.583-2.625 Å, the bond distances fell in range of 2.207-2.246 Å between Dy(III) ion and ligand oxygen atoms, and the bond length between Dy(III) ion and coordinated Cl^- ion was 2.682 Å. Based on *SHAPE* analysis, the calculated result suggested that the seven coordinated Dy^{III} cores could be viewed as capped trigonal prism geometry (Table S16). The supramolecular weak action of **Br3-1** structure contains C-H···O, C-H···Br, C-H···π and π···π, respectively, which

bond distances are C-H···O (2.591 Å), C-H···Br (2.4806 Å), C-H···π (3.690 Å) and π···π (3.666, 3.719 and 3.751 Å) (Figure S22, Table S17). The supramolecular weak action distances were all within a reasonable range and could thus be considered to form a 14-connected ***fcu*** nets with distances of 8.554 ~ 13.789 Å between the centers of the Dy-HOFs (Figure S22e).

Table S16. *SHAPE* analysis of the Dy^{III} ion in **Br3-1**.

Label	Shape	Symmetry	Distortion(τ)
HP-7	D_{7h}	Heptagon	30.892
HPY-7	C_{6v}	Hexagonal pyramid	18.692
PBPY-7	D_{5h}	Pentagonal bipyramid	5.617
COC-7	C_{3v}	Capped octahedron	2.976
CTPR-7	C_{2v}	Capped trigonal prism	2.008
JPBPY-7	D_{5h}	Johnson pentagonal bipyramid J13	11.014
JETPY-7	C_{3v}	Johnson elongated triangular pyramid J7	16.648

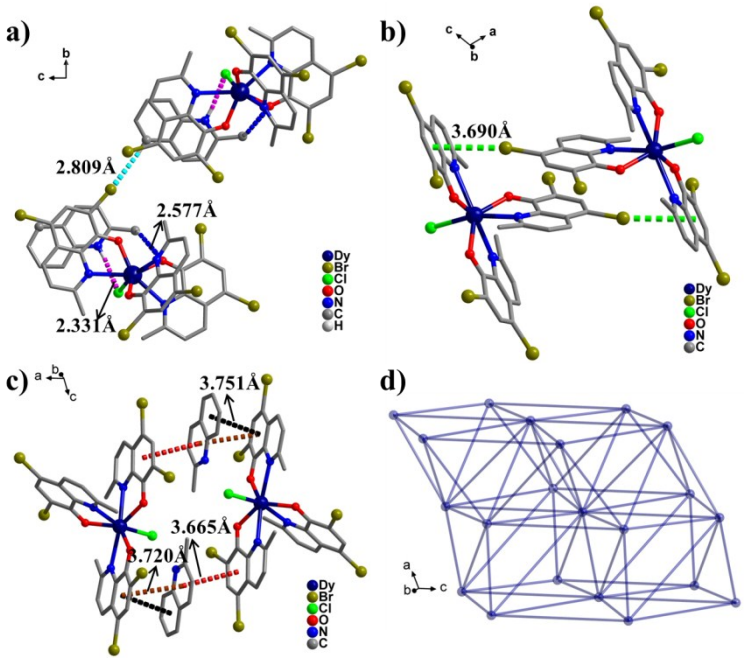

Figure S22. (a, b, c) Structure of **Br3-1** showing the supramolecular interactions; (d) The connecting modes of the clusters through π···π interactions and hydrogen bonds in **Br3-1**.

Table S17. Hydrogen-bond and C-Br···π bond geometries and π···π interactions for **Br3-1**.

Hydrogen bond	Distance[a], Å	Angle[b], °
C_{31}–H_{31C}···O_1	2.591	149
C_{36}–H_{36}···Br_6	2.806	155
π···π	**Distance[c], Å**	**Distance[d], Å**
π(Ph)··· π(Ph)	3.751(4)	3.509(2)

π(Ph)··· π(PhC5N)	3.719(4)	3.509(2)
π(Ph)···π(PhC5N)	3.666(4)	3.563(2)
C–X···π	**Distance[c], Å**	**Angle[e], °**
C_{16}–Br_3···π(Ph)	3.690(2)	170.2

[a] Distance between acceptor and donor; [b] Angle of acceptor–hydrogen–donor; [c] Centroid–to–centroid distance; [d] Interplanar distance; [e] Angle of carbon–hydrogen–centroid.

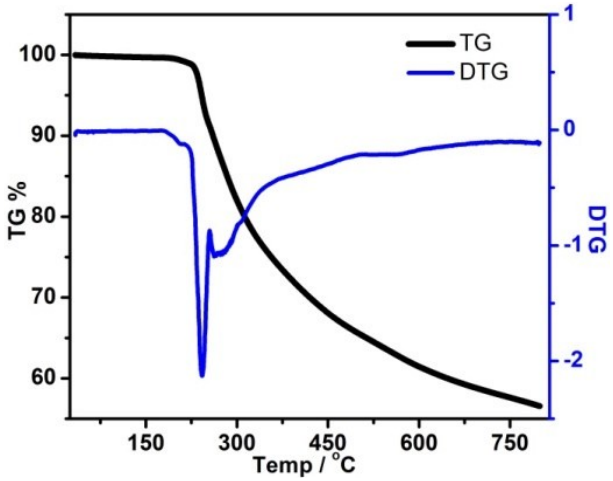

Figure S23. Thermogravimetry of **Br3-1** at a heating rate of 5 °C/min under N_2 atmosphere.

The magnetic susceptibilities of polycrystalline samples of **Br3-1** were measured on direct-current field of 1000 Oe upon cooling from 300 to 2 K (Figure S24). The values of $\chi_m T$ were normal, which are slightly lower than the expected value of 14.17 $cm^3 \cdot K \cdot mol^{-1}$ for one uncorrelated Dy(III) ion ($^6H_{15/2}$, g = 4/3).[5] The non-superposition of M and H/T data were showed in Figure S25.

The ac-susceptibilities were studied through three sets of measurements as a function of temperature for a range of frequencies spanning 10−1000 Hz by using an oscillating field of 2.5 Oe in 0 and 2000 Oe bias dc−field for **Br3-1** and **Br3-3**. The analysis of magnetic data of **Br3-1** showed that it exhibited clearly field-induced single-molecule-magnetic behavior (Figure S26a and S26c). After testing the ground sample, it was found that the single-molecule magnetic behavior of **Br3-3** was similar. There was a very evident field-induced slow relaxation phenomenon (Figure S26b and S26d).[8]

The Cole-Cole plots (Figure S27-28 for **Br3-1** and **Br3-3**) followed a single relaxation Debye model. The fitting parameters τ (relaxation time) and α (α determines the width of the distribution of relaxation times) were listed in Table S18-S19. The parameter α for all Dy-HOFs fell in the range of 0.2~0.5, suggesting a narrow-to-moderate distribution of magnetic relaxation. Temperature dependent relaxation time was analyzed assuming a thermally activated process following the Arrhenius law ($\tau = \tau_0 \exp(U_{eff}/k_B T)$). The energy barriers and extrapolated relaxation times were U_{eff} = 56.3 K and $\tau_0 = 1.4 \times 10^{-10}$ s for **Br3-1**, and U_{eff} = 0.8 K and $\tau_0 = 5.5 \times 10^{-4}$ s for **Br3-3** under 2000 Oe dc field (Figure S27d, 28d).

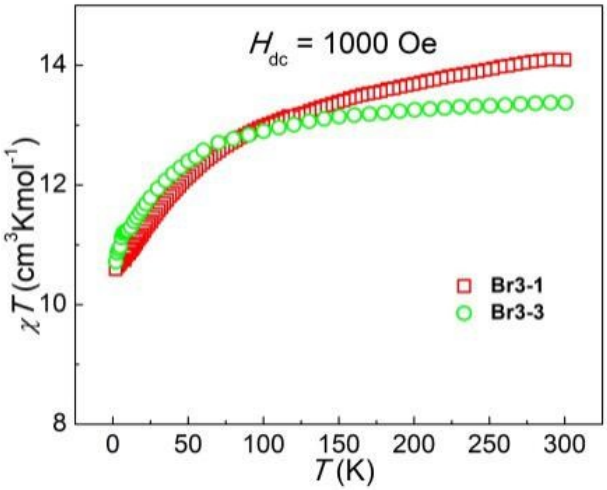

Figure S24. Temperature dependence of $\chi_m T$ for **Br3-1** and **Br3-3**.

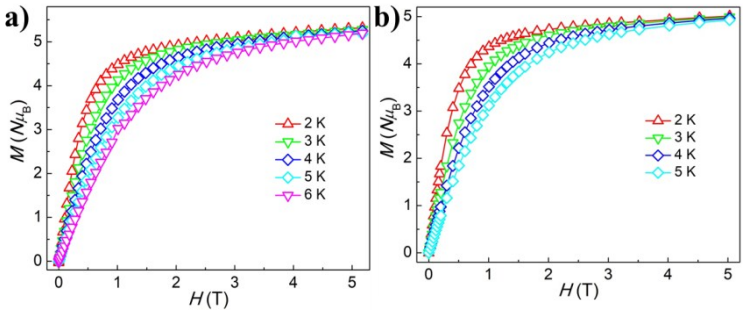

Figure S25. Field dependence of the magnetization for **Br3-1** (a) and **Br3-3** (b) at 2-6 K.

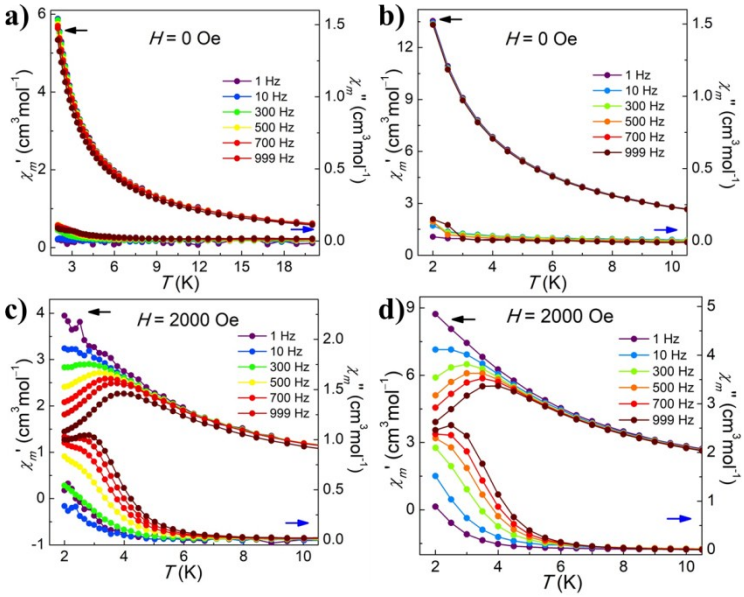

Figure 26. The temperature dependence of the in-phase (χ') and out-of-phase (χ'') ac-susceptibilities for different frequencies in 0 and 2000 Oe dc-field for **Br3-1** (a and c) and **Br3-3** (b and d).

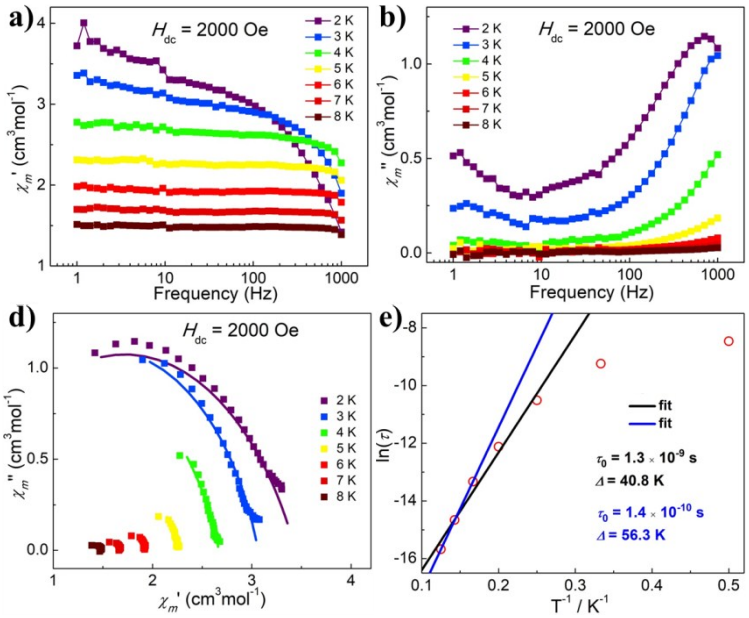

Figure S27. Variable-frequency dependent ac susceptibilities and Cole-Cole plots from ac-susceptibilities for **Br3-1** (a, b and c) under 2000 Oe dc-field, and Arrhenius plots generated from the temperature-dependent relaxation times extracted from the ac-susceptibilities Cole-Cole fits for **Br3-1** (d).

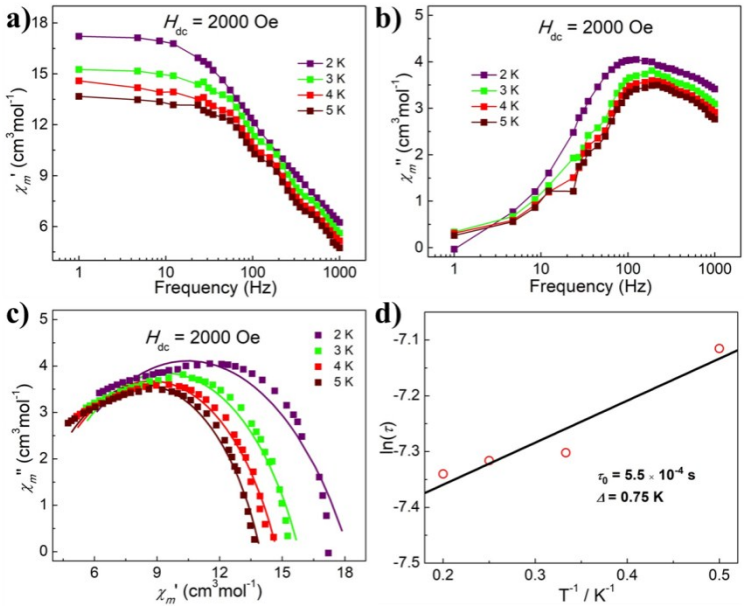

Figure S28. Variable-frequency dependent ac susceptibilities and Cole-Cole plots from ac-susceptibilities for **Br3-3** (a, b and c) under 2000 Oe dc-field, and Arrhenius plots generated from the temperature-dependent relaxation times extracted from the ac-susceptibilities Cole-Cole fits for **Br3-3** (d).

Table S18. Selected parameters from the fitting results of the Cole-Cole plots for **Br3-1** under 2000 Oe field.

	Br3-1		
T (K)	τ	α	residual
2	2.12E-04	2.89E-01	2.69E-01
3	9.69E-05	2.09E-01	9.87E-02
4	2.72E-05	2.20E-01	1.85E-02
5	5.45E-06	3.27E-01	1.08E-02
6	1.63E-06	3.64E-01	1.04E-02
7	4.30E-07	4.42E-01	7.48E-03
8	1.56E-07	4.94E-01	6.29E-03

Table S19. Selected parameters from the fitting results of the Cole-Cole plots for **Br3-3** under 2000 Oe field.

	Br3-3		
T (K)	τ	α	residual
2	8.13E-04	3.75E-01	3.15E+00
3	6.74E-04	3.13E-01	1.85E+00
4	6.65E-04	3.01E-01	1.47E+00
5	6.49E-04	2.76E-01	1.63E+00

References

[1] G. M. Sheldrick, SHELXT: Integrated space-group and crystalstructure Determination. *Acta Crystallogr., Sect. C: Struct. Chem*. 2015, **71**, 3-8.

[2] B. Chattopadhyay, A. K. Mukherjee, N. Narendra, H. P. Hemantha, V. V. Sureshbabu, M. Helliwell and M. Mukherjee, *Cryst. Growth Des*., 2010, **10**, 4476–4484.

[3] S. K. Seth†, D. Sarkar, A. D. Jana and T. Kar, *Cryst. Growth Des*., 2011, **11**, 4837–4849.

[4] A. D. Martin, J. Britton, T. L. Easun, A. J. Blake, W. Lewis and M. Schröder, *Cryst. Growth Des*., 2015, **15**, 1697–1706.

[5] C. Benelli and D. Gatteschi, *Chem. Rev*. 2002, **102**, 2369−2387.

[6] a) Y. Bi, Y.-N. Guo, L. Zhao, Y. Guo, S.-Y. Lin, S.-D. Jiang, J. Tang, B.-W. Wang and S. Gao, *Chem. Eur. J*. 2011, **17**, 12476–12481; b) C. L. F. Wang, J.-Z. Qiu, J.-L. Liu, Y.-C. Chen, J.-H. Jia, J. Jover, E. Ruiz and M.-L. Tong, *Chem. Commun*. 2015, **51**, 15358–15361; c) M. Ren, S.-S. Bao, B.-W. Wang, R. A. S. Ferreira, L.-M. Zheng and L. D. Carlos, *Inorg. Chem. Front*. 2015, **2**, 558–566; d) X.-D. Huang, Y. Xu, K. Fan, S.-S. Bao, M. Kurmoo and L.-M. Zheng, *Angew. Chem. Int. Ed*. 2018, **57**, 8577 –8581; e) J. Wu, M. Guo, X.-L. Li, L. Zhao, Q.-F. Sun, R. A. Layfield and J. Tang, *Chem. Commun.* 2018, **54**, 12097–12100.

[7] a) P. Zhang, M. Perfetti, M. Kern, P. P. Hallmen, L. Ungur, S. Lenz, M. R. Ringenberg, W. Frey, H. Stoll, G. Rauhut and J. van Slageren, *Chem. Sci*., 2018, **9**, 1221–1230; b) X.-Q. Ji, F. Ma, J. Xiong, J. Yang, H.-L. Sun, Y.-Q. Zhang and S. Gao, *Inorg. Chem. Front*., 2019, **6**, 786–790; c) W.-Y. Zhang, Y.-Q. Zhang, S.-D. Jiang, W.-B. Sun, H.-F. Li, B.-W. Wang, P. Chen, P.-F. Yan and S. Gao, *Inorg. Chem. Front*., 2018, **5**, 1575–1586.

[8] X. D. Huang, M. Kurmoo, S. S. Bao, K. Fan, Y. Xu, Z. B. Hu and L. M. Zheng, *Chem. Commun*., 2018, **54**, 3278–3281.

[9] F. Aquilante, J. Autschbach, R. K. Carlson, L. F. Chibotaru, M. G. Delcey, L. De Vico, I. Fdez. Galván, N. Ferré, L. M. Frutos, L. Gagliardi, M. Garavelli, A. Giussani, C. E. Hoyer, G. Li Manni, H. Lischka, D. Ma, P. Å. Malmqvist, T.

Müller, A. Nenov, M. Olivucci, T. B. Pedersen, D. Peng, F. Plasser, B. Pritchard, M. Reiher, I. Rivalta, I. Schapiro, J. Segarra-Martí, M. Stenrup, D. G. Truhlar, L. Ungur, A. Valentini, S. Vancoillie, V. Veryazov, V. P. Vysotskiy, O. Weingart, F. Zapata and R. Lindh, MOLCAS 8: New Capabilities for Multiconfigurational Quantum Chemical Calculations across the Periodic Table, *J. Comput. Chem*., 2016, **37**, 506-541.

[10] a) L. F. Chibotaru, L. Ungur and A. Soncini, *Angew. Chem. Int. Ed.*, 2008, **47**, 4126–4129. (b) L. Ungur, W. Van den Heuvel and L. F. Chibotaru, *New J. Chem.*, 2009, **33**, 1224–1230. (c) L. F. Chibotaru, L. Ungur, C. Aronica, H. Elmoll, G. Pilet and D. Luneau, *J. Am. Chem. Soc.*, 2008, **130**, 12445–12455.

[11] Z.-H. Zhu, X.-F. Ma, H.-L. Wang, H.-H. Zou, K.-Q. Mo, Y.-Q. Zhang, Q.-Z. Yang, B. Li and F.-P. Liang, *Inorg. Chem. Front.* 2018, **5**, 3155–3162.

[12] A. Kirchon, L. Feng, H. F. Drake, E. A. Joseph and H.-C. Zhou, *Chem. Soc. Rev.* 2018, **47**, 8611–8638.